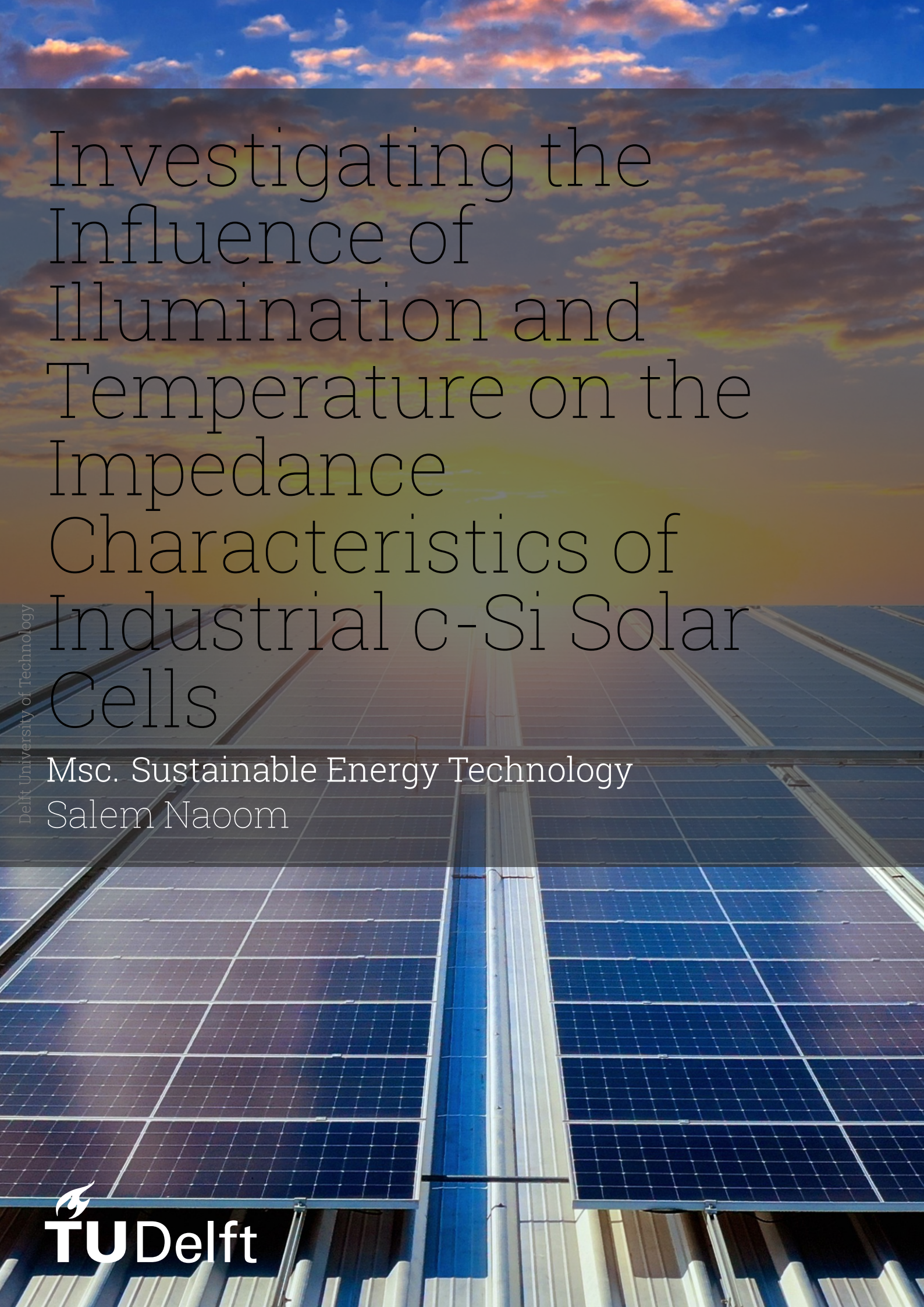

Investigating the Influence of Illumination and Temperature on the Impedance Characteristics of Industrial c-Si Solar Cells

Msc. Sustainable Energy Technology

Salem Naoom

Delft University of Technology

TU Delft

Investigating the Influence of Illumination and Temperature on the Impedance Characteristics of Industrial c-Si Solar Cells

by

Salem Naoom

Student number: 5654963

Project Duration: December, 2022 - September, 2023

Thesis committee: Prof. Dr. Ivan Gordon
Dr. Milos Cvetkovic
Dr. Patrizio Manganiello
Ir. David van Nijen

TU Delft

Preface

This master thesis marks the culmination of my educational journey, which began 22 years ago when I started school in my home country, Iraq. Over these years, I have witnessed numerous significant events. In 2003, a war began in my country, and since then, life there has become unsafe. Despite the challenging circumstances, I persevered, attending school even in unsafe conditions. In 2012, me and my family had the opportunity to travel to the Netherlands and start a new life. My initial challenge was to master the Dutch language in order to continue my education. Subsequently, I faced the formidable task of enrolling in high school (VWO) despite my limited Dutch proficiency. Eventually, I overcame this hurdle and successfully completed high school, paving the way for my next adventure: pursuing a degree in electrical engineering at the University of Twente. After completing my bachelor study, I decided to contribute to the future of renewable energy and chose to specialize in Sustainable Energy Technology for my master's studies. During my master, I have learnt a lot about the renewable energy, with a particular focus on solar systems. Given my strong passion for solar energy, I decided to carry out my thesis project with the PVMD group.

My thesis project aimed to study and analyze the impact of temperature and illumination levels on solar cell impedance. I am grateful for this thesis topic as it combines both my knowledge in electrical engineering and my passion for solar energy. Over the last 9 months, I have learned a lot and was able to laminate solar cells myself. Furthermore, I had the opportunity to visit Imec in Belgium, one of the famous international R&D organizations.

Personally, I would like to thank my daily supervisor David van Nijen for his help. He has given me guidance during the project and shared a lot of valuable insights. Furthermore, I would like to thank Mirco Muttillo for building the experimental setup and helping me to work with it. In addition, I would like to thank Patrizio Manganiello for his help during our meetings and the positive energy I was receiving during our talks.

Finally, I would like to thank my family for everything they have done for me during all the years, for their support and being always there for me.

Salem Naoom
Delft, September 2023

Abstract

Partial shading poses a significant challenge in the photovoltaic (PV) technology sector, potentially leading to a considerable drop in energy production. To address this issue, sub-module Maximum Power Point Tracking (MPPT) devices have been developed and employed. In such devices, capacitors are used at the input to mitigate input voltage ripples. In order to reduce the amount of circuit components and potentially increase the reliability of the these devices, there is a proposal to substitute the input capacitor of the sub-module MPPT device with the capacitance of the PV cell or PV cell string. While this may seem like a viable solution, PV cell capacitances may not be suitable for this purpose due to their sensitivity to temperature and illumination levels. This sensitivity can result in a mismatch between the PV cell and the sub-module MPPT. In addition to sub-module MPPT, the PV cell capacitance could also be important for other applications such as visible light communication and determination of the minimum required I-V measurement scan time. Therefore, this thesis project aims to investigate the influence of temperature and illumination levels on PV cell impedance.

To assess the impedance of the PV cell, we employed an impedance spectroscopy (IS) setup. Subsequently, a series of experiments were conducted under varying temperature and illumination conditions, involving two distinct PV cell types: Interdigitated Back Contact (IBC) and Passivated Emitter and Rear Contact (PERC). Moreover, we utilized the Complex Nonlinear Least Squares (CNLS) algorithm alongside an electrical equivalent model designed for PV cell impedances to accurately fit the impedance data.

In the initial phase of this thesis project, we conducted a temperature experiment. For both cells, the PV cell impedance has been measured at various temperatures. From this experiment, it was concluded that in dark conditions and at 619.5mV (maximum power point voltage at STC), the PV cell capacitance of IBC cell increased from 7.6mF at 25°C to 22mF at 60°C. Furthermore, the capacitance of PERC cell in dark conditions and at 539mV (maximum power point voltage at STC) increased from 0.19mF to 2.4mF at 25°C and 55°C, respectively. These findings highlight the temperature-dependent behavior of PV cell capacitance for both IBC and PERC cells which is related to the cahnge in the intrinsic carrier concentration (n_i).

In the second phase of this thesis project, we conducted an illumination experiment. From this experiment, it was observed that the capacitance of the IBC cell at 30°C and 619.5mV increased from 9.2mF in absence of light to 13.8mF at 500W/m^2. Similarly, for PERC cell, the capacitance at 30°C and 539mV increased from 0.3mF in dark conditions to 0.7mF at 700W/m^2. These findings indicate that the capacitance of both cell types is influenced by the level of illumination, with higher light intensity leading to increased capacitance values which is related to the increase in the PN junction voltage.

In the third phase of this thesis project, we conducted an experiment which aimed to investigate the combined impact of temperature and illumination on the PV cell capacitance at varying maximum power point voltages. In this experiment, it was observed that at 30°C $<$ T $<$ 60°C and 100W/m^2 $<$ intensity $<$ 500W/m^2, the capacitance of IBC cell varies between 3 and 9.5mF for IBC cell, while it operates between 0.045 to 0.25mF for PERC cell. Additionally, it was noted that the illumination in this experiment has more impact on the PV cell capacitance than the temperature as the maximum power point voltage increases significantly with increasing intensity, whereas it decreases with increasing temperature.

Based on the findings from the experiments discussed above, it becomes evident that the capacitance of PV cells undergoes fluctuations in response to changes in temperature and illumination levels. Upon comparing the data obtained from the characterized IBC and PERC cells, we can draw the conclusion that a single IBC cell exhibits a greater potential than a single PERC cell when it comes to substituting the input capacitor of a power converter and effectively performing this role. This is due to the fact

that the capacitance of an individual IBC cell exceeds that of a single PERC cell. Nevertheless, in the case of a PERC cell string, the capacitance may be sufficiently high to function as an input capacitor even under conditions of low illumination and low temperatures.

Contents

Nomenclature

Abbreviations

Abbreviation	Definition
AC	alternating current
AM	air mass
ARC	anti reflecting coating
BSF	back surface field
CNLS	complex nonlinear least-squares
CP	current probe
c-Si	crystalline silicon
CPE	constant phase element
DC	direct current
ESP	electrical sustainable power
FF	fill factor
FG	function generator
GHG	greenhouse gas
IBC	interdigitated back contact
IS	impedance spectroscopy
LA	lock-in amplifier
LED	light-emitting diode
LH	low-high junction
MPP	maximum power point
MPPT	maximum power point tracking
op-amp	operational amplifier
PERC	passivation emitter rear contact
PN	p- and n-type junction
PS	power supply
PV	photovoltaic
SCR	space charge region
SMU	source measurment unit
STC	standard test condition

Symbols

Symbol	Definition	Unit
f	frequency	[Hz]
η	efficiency	[%]
I_{sc}	short circuit current	[A]
J_0	saturation current density	[mA/cm^2]
J_{ph}	photocurrent density	[mA/cm^2]
J_{sh}	short circuit current density	[mA/cm^2]
R_s	series resistance	[Ω]
R_{sh}	shunt resistance	[Ω]
T	temperature	[K]
V_{oc}	open circuit voltage	[V]

1 Introduction

This chapter serves as an introduction, providing context for the thesis and giving a detailed overview of the project. It uses some technical terms commonly used in photovoltaics, which will be further explained in chapter 2. This chapter is organized as follows: Section 1.1 addresses the need for solar energy and PV modules. In section 1.2, the subject of partial shading is introduced. Possible solutions for shading are presented in section 1.3. Then, a brief overview of a specific boost converter circuit and solar cell's equivalent circuit is provided in section 1.4. The effect of temperature and illumination on PV cell performance is illustrated in section 1.5. The final section, 1.6, outlines the objectives of the project and provides a description of the project.

1.1. Solar energy and PV modules

Energy is essential for our daily lives and has been used in various forms such as thermal, chemical, and electrical for many years. In 2021, humans have consumed around 176 PWh of primary energy, out of which 136 PWh came from fossil fuels (non-renewable energy sources), which is equivalent to 77% of the total consumed energy [1]. Being heavily dependent on fossil fuels is a significant risk for the future generations. Furthermore, burning fossil fuels increases the concentration of greenhouse gases (GHG) in the Earth's atmosphere, which leads to global warming by trapping heat from the sun and preventing it from escaping into space [2]. Additionally, fossil fuels are limited resources and will eventually run out [1]. Figure 1.1 illustrates the remaining time for consumption of coal, oil, and natural gas based on the present annual production levels and known reserves.

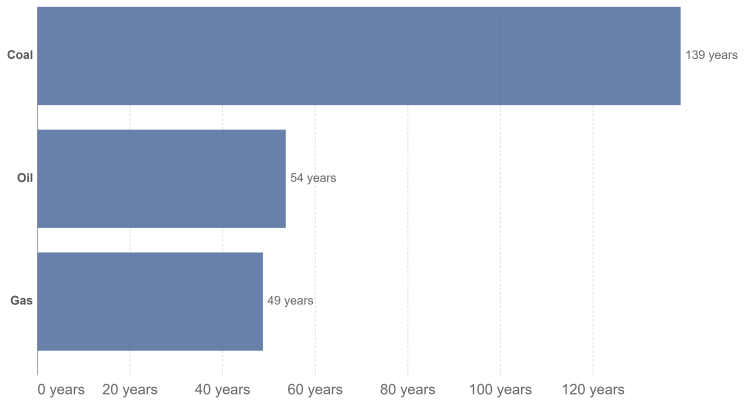

Figure 1.1: Years of fossil fuels reserves left [1].

As a result of these concerns, it is necessary to find alternative energy sources, specifically renewable energy sources. Solar energy is one such renewable energy source that has high potential [3]. Inside the sun, a nuclear fusion reaction takes place continually, releasing energy in the form of heat and light. The amount of solar energy incident on Earth is around 10,000 times larger than the total energy

consumption of mankind [3]. Therefore, Photovoltaic (PV) technology appears to be a promising solution to replace non-renewable energy sources. However, PV modules are far from perfect and their performance could be affected in real-life conditions by the temperature and illumination [3]. Therefore, it is essential to understand the behavior of PV modules under real-life conditions to improve their efficiency and performance. One of the situations where the performance of PV modules reduces is when the PV module is partially shaded. In the following sections, the shading issue will be introduced and explained in more details .

1.2. Partial shading

Partial shading refers to the phenomenon where only a portion of a PV module is shaded, rather than the entire module. This can occur due to a variety of factors, such as nearby buildings, trees, or other structures that block some of the sunlight from reaching the module. When a PV module is partially shaded, it can result in a significant reduction in power output, as the shaded cells are not able to generate electricity. Engineers often install PV modules on the roofs of houses and buildings in locations that are not shaded in order to maximize the energy generation. However, this is not always feasible as the sun's position changes throughout the year due to the Earth's orbit. This means that an area may be shaded during the winter but not during the summer, or vice versa. To illustrate the effect of shading, consider Figure 1.2 which shows a string of 6 series-connected solar cells of which one is shaded. When a single cell is shaded, it reduces or eliminates the current it generates. This impacts the entire string of cells as they are connected in series, where the current should be consistent across all cells. As a result, the current generated by the entire string is limited to the current generated by the shaded cell, and the power generated is also reduced. On the other hand, the shading of a single cell could lead to a different impact, where the string is operating at a normal current but the shaded cell operates in breakdown condition. In this case, a high fraction of the generated power by the string will be dissipated over the shaded cell [3]. To address shading issues, two different techniques have been developed and will be discussed in the following section.

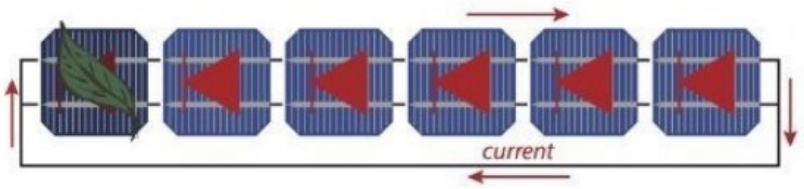

Figure 1.2: A string of 6 solar cells of which one is shaded [3].

1.3. Possible solutions for shading

As discussed before, shading can greatly impact the power generated by a solar system. To address this, two techniques are commonly used to reduce power losses. The first technique is the use of bypass diodes [3]. Typically, a PV module comprises a series connection of 60-72 PV cells, arranged in three submodules of 20–24 cells, and a total of three bypass diodes [4]. Figure 1.3 illustrates the same simple string shown before with integrated bypass diodes for each cell. The yellow dashed line shows the path of the current when a cell is shaded, allowing the current to bypass the shaded cell and optimize power generation.

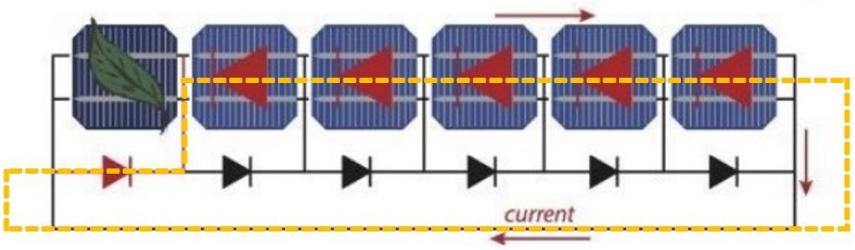

Figure 1.3: A string of 6 solar cells of which one is shaded [3].

The second technique to reduce the power losses due to shading is by implementing maximum power point tracking (MPPT) on a sub-module level [5, 6, 7]. This enables the adjustment of the operating point of one or a group of solar cells without impacting the performance of the other cells in the PV module. In order to achieve a high performance in such power conditioning circuits, the design of the converter should be matched with the PV cell impedance at the input [8]. Therefore, it is important to study the behavior of the impedance inside the PV cells.
The input capacitor of the power converters is an indispensable component as it reduces the ripple voltage at the converter's input [9]. However, it is one of the least reliable components in power converters [10]. According to [11, 12], the self-capacitance of the PV cells is able to fulfil the function of the input capacitor in sub-module MPPT. This will eventually reduce the amount of the used capacitors in the power converters and enhances the reliability of the converter. In the next section, an example of a converter circuit will be presented to illustrate the new configuration of the converter circuit once it is connected to a PV cell.

1.4. Boost converter circuit and equivalent circuit of a solar cell

A boost converter circuit is a commonly used circuit in PV systems. A boost converter is a type of DC-DC power converter that increases the voltage of a direct current (DC) input voltage. This could be done by storing energy in an inductor and then releasing it to the output at a higher voltage. A boost converter consists of several components, including an inductor, capacitors, a diode (or transistor), and a switching element (such as a transistor) as shown in Figure 1.4. The goal of using this converter is to increase and fix the output voltage of the PV module in order to connect it with a DC-AC converter or a battery.

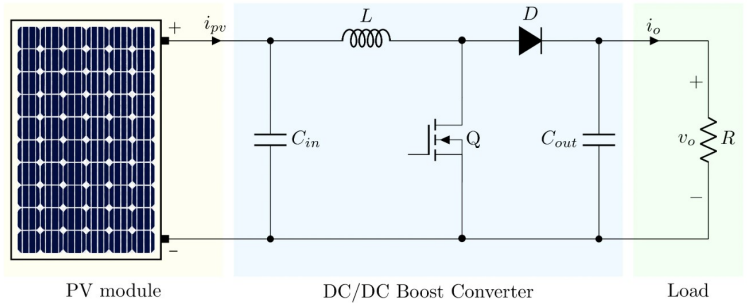

Figure 1.4: PV module connected with a boost converter [13].

The PV module in Figure 1.4 can be represented by its equivalent circuit, as shown in Figure 1.5. This circuit is explained in more detail in chapter 2. In Figure 1.5, a component called the PV cell capacitance (C_d) is present. This capacitor plays a dominant role when the operating PV cell voltage is close to or greater than the maximum power point voltage (V_{mpp}) and can have a significant value. Therefore, in theory, C_d could replace C_{in} that is shown in Figure 1.4 according to [11, 12].

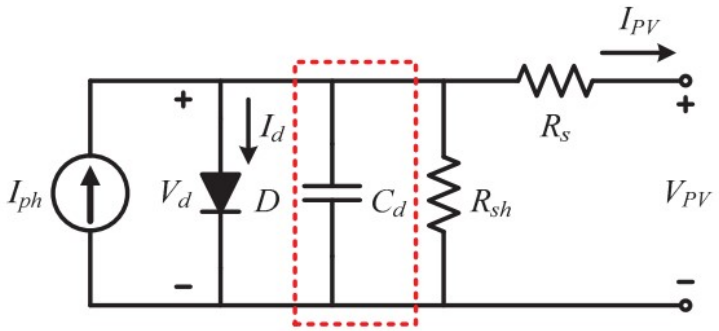

Figure 1.5: Equivalent circuit of a PV cell [12].

A PV module generally consists of multiple PV cells connected together. These cells are connected by metal wires, which have resistance and parasitic inductive impedance which becomes higher, particularly at high frequencies [12]. Similarly to the self-capacitance of the PV cell, there might be a potential to replace the inductor of the converter with the parasitic inductances of the wires if the PV inductance is high enough. If this is done, the final circuit will appear as shown in Figure 1.6.

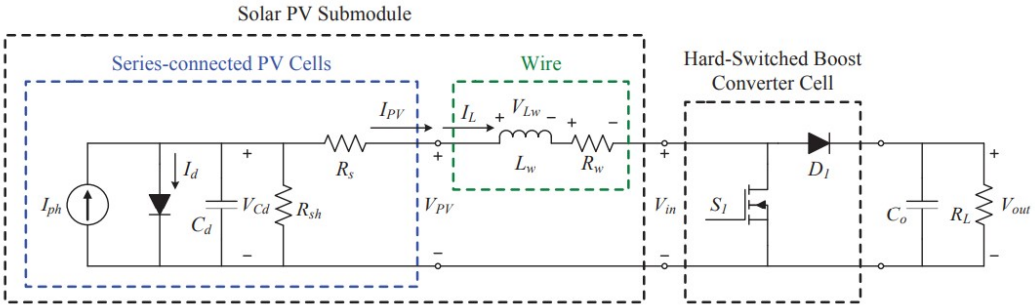

Figure 1.6: The circuit diagram of the proposed solar cell with the integrated boost converter [12].

1.5. Effect of temperature and illumination on PV cell performance

PV cells are devices designed to convert solar energy into electrical power. However, the amount of electricity generated by PV cells is subject to significant variability, which is dependent on several factors. In real-life operating conditions, the performance of a PV cell is primarily influenced by temperature and illumination levels [3]. The effect of temperature and irradiance on the I-V curve is illustrated in Figure 1.7, where the I-V curve under standard test conditions (black) is compared to the I-V curve under increased temperature (red) and irradiance (blue). As shown in Figure 1.7, the short circuit current of the PV cell increases with rising temperature, while the open circuit voltage decreases. Moreover, both the short circuit current and open circuit voltage rise with increasing irradiance [3]. Such changes can have a significant impact on the impedance of the PV cell. Therefore, it is imperative to investigate the effect of real-life operating conditions on the PV cell's performance to ensure efficient application of the MPPT sub-module technique.

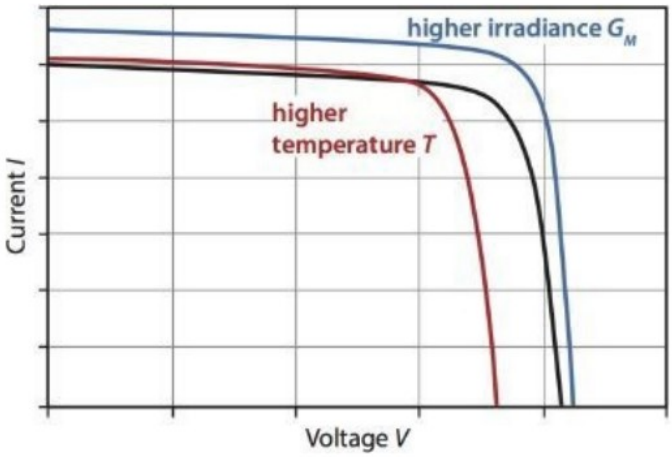

Figure 1.7: Effect of a temperature and irradiance increase on the I-V PV cell characteristic [3].

1.6. Project description and outline

This thesis project aims to examine the behavior of the impedance of a commercial PV cell under real-world operating conditions. The main research question of this project is:

How does the impedance of industrial c-Si PV cells vary at different temperature and illumination levels?

To answer this question, the following research objectives have been developed:

1. Determine the appropriate impedance model that accurately characterizes the dynamic electrical behavior of industrial c-Si PV cells under real-world operating conditions.
2. Assess the impact of temperature on the impedance of a single PV cell.
3. Investigate how the impedance of a single PV cell changes under varying illumination levels.
4. Examine the impact of temperature and illumination on the impedance of a PV cell at its maximum power point.

Now that the reader has been introduced to the research topic, chapter two thoroughly treats the theoretical background. The following chapter, chapter three, details the method used to execute the experiments in the laboratory. Then, chapter four will introduce and discuss the results obtained from the experiments. Finally, a conclusion of the thesis project will be discussed in chapter five.

2

Theoretical Background

In this chapter, some theoretical information will be presented. The chapter is divided into five sections. In section 2.1, the working principle of the PV cell will be discussed. Section 2.2 will introduce the PV cell parameters. Additionally, the equivalent circuit of the PV cell in steady-state mode will be presented and explained in section 2.3. Then, in section 2.4, the equivalent circuit of the PV cell in alternating current (AC) mode will be developed and explained. Finally, the concept of constant phase element will be introduced and discussed in section 2.5.

2.1. The working principle of the PV cell

As discussed earlier, the sun provides the Earth with energy in forms of light and heat. This energy transfers from the sun and penetrates the atmosphere of the Earth. In 1905, Albert Einstein defined the light as energy quanta, called photons [3]. The energy of a photon can be expressed as $E_{ph} = hv$, where h is Planck's constant and v is the frequency of the light. E_{ph} can generate a potential difference at the junction of two different semiconductor materials. The working principle of PV cells is based on this operation which is called the photovoltaic effect. Note that many of the information in this section was taken from the book Solar Energy written by Smets et al. [3]. The photovoltaic effect consists of three basic processes:

1. **Generation of charge carriers due to the absorption of photons**
   The PV cells consist mainly of semiconductor materials. Semiconductor materials are materials that have electrical conductivity between that of a conductor and an insulator. To increase the conductivity of a semiconductor, additional energy is required. By absorption of a photon in a semiconductor material, the photon energy will be used to excite an electron from an energy level called the valence band (E_v) to a higher energy level called the conduction band (E_c). The energy difference between E_c and E_v is called the bandgap energy (E_g) and can be expressed as $E_g = E_c\text{-}E_v$. So, in order to excite and electron, the photon energy must be equal to or higher than the bandgap energy: $E_{ph} \geq E_g$. Once this condition is fulfilled, an electron-hole pair will be generated as shown in Figure 2.1 (at 1).
2. **Subsequent separation of the photo-generated charge carriers in the junction**
   Typically, when a photon is absorbed by a semiconductor, it causes an electron in the valence band to be excited to a higher energy level in the conduction band, creating an electron-hole pair. However, this excited state is not permanent, and the electron will eventually fall back to its initial energy level, releasing the energy in the process as illustrated in Figure 2.1 (at 2). This release of energy can take the form of a photon of light (radiative recombination) or be transferred to other electrons, holes, or lattice vibrations (non-radiative recombination).

   If the energy stored in the electron-hole pair is to be used to perform work in an external circuit, such as powering an electrical device, special structures called semipermeable membranes must be present on both sides of the absorber. These membranes allow for the flow of electrons out of one side and holes out of the other side, allowing for the separation of the electron-hole

pairs and the conversion of their energy into usable electrical power as can be seen in Figure 2.1 (at 3). These membranes are typically made of n- (doped with electrons) and p-type (doped with holes) materials and are commonly used in most PV cells.

To minimize the effect of recombination, the PV cell must be designed in such a way that the electrons and holes can reach the membranes before they recombine. So, the time it requires the charge carriers to reach the membranes must be shorter than their lifetime. This requirement limits the thickness of the absorber.

3. **Collection of the photo-generated charge carriers at the terminals of the junction** The final step in the process of converting the energy from absorbed sunlight into usable electrical power is the extraction of charge carriers from the PV cell with electrical contacts. This allows for the charge carriers to perform work in an external circuit (see Figure 2.1 (at 4)), converting the chemical energy of the electron-hole pairs into electric energy. After passing through the circuit, the electrons recombine with holes at a metal-absorber interface as illustrated in Figure 2.1 (at 5).

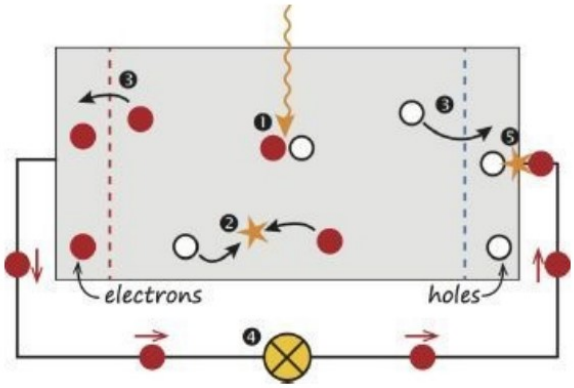

Figure 2.1: A simple PV cell model to illustrate the working principle of the PV cells [3].

2.2. PV cell parameters

To determine the efficiency of a PV cell, some PV cell parameters are typically used. In this section, these parameters will be introduced and explained. Again, many of the information in this section was taken from the book Solar Energy written by Smets et al. [3].

2.2.1. Short circuit current density

As is known, PV cells generate current when the cells are exposed to light or sun. The amount of generated current depends on the photon flux incident on the PV cell. When the electrodes of the PV cell are connected together, short circuited, the current that flows through the external circuit is called short circuit current (I_{sc}). By using I_{sc}, one can determine the maximum current (I_{mpp}) that can be delivered and used by a PV cell from the AM1.5 spectrum[1]. Since I_{sc} depends on the area of the cell, and each cell has a different area, scientists and manufacturers tend to use the short circuit current density J_{sc} (mA/cm^2) which is independent of the cell area.

2.2.2. Open circuit voltage

The open-circuit voltage V_{oc} is the voltage at which no current flows through the external circuit. It is the maximum voltage that a PV cell can deliver. The V_{oc} is a measure of the difference between the quasi-Fermi levels of electrons (E_{Fn}) and holes (E_{Fp}). The difference between E_{Fn} and E_{Fp} is always smaller than the corresponded voltage of the band gap, therefore qV_{oc} cannot be higher than the band gap of a material. The V_{oc} can be calculated with equation 2.1:

$$V_{oc} \approx \frac{k_B T}{q} \ln\left(\frac{J_{ph}}{J_0}\right) \tag{2.1}$$

where, k_B is Boltzmann constant, T the temperature, q the elementary charge, J_{ph} the photo generated current (or photocurrent) density and J_0 the saturation current (or dark current) density.

Equation 2.1 shows that V_{oc} depends on J_{ph} and J_0. Since J_{ph} has a small variation, J_0 has the key effect on the V_{oc} as it can vary in orders of magnitude. Furthermore, J_0 depends on the recombination in the PV cell, therefore V_{oc} is considered as a measure of the amount of recombination in the device.

2.2.3. Fill factor

A PV cell can operate at different power levels depending on the amount of exposed light and temperature. When the PV cell operates at its maximum power, then the operation point is called the maximum power point P_{mpp}. The fill factor is the ratio between the maximum power ($P_{mpp} = J_{mpp}V_{mpp}$) generated by a PV cell and the product of V_{oc} with J_{sc} as is shown in equation 2.2:

$$FF = \frac{J_{mpp}V_{mpp}}{J_{sc}V_{oc}} \tag{2.2}$$

2.2.4. Efficiency

The efficiency of a PV cell is the ratio between the maximum generated power P_{mpp} and the incident power P_{in}. The PV cells are always tested under the standard test conditions (STC). So, the incident light is described by the AM1.5 spectrum, the irradiance (P_{in}) is 1000 W/m^2 and the cell temperature is 25°C. The efficiency can be calculated using equation 2.3:

$$\eta = \frac{P_{mpp}}{P_{in}} = \frac{J_{sc}V_{oc}FF}{P_{in}} \tag{2.3}$$

[1]The AM1.5 spectrum is a standard way of measuring the intensity of light from the sun that is used in the International Standard IEC 60904-3. It serves as a reference for the distribution of solar radiation and used to compare different PV cells.

2.3. Equivalent circuit of PV cell in steady-state mode

In this section, the focus will be on analyzing the electrical behavior of a PV cell by examining its equivalent circuit. The discussion will include the examination of both the ideal and non-ideal versions of the one-diode model, as well as the introduction and explanation of the non-ideal two-diodes model. Additionally, the technology of back surface field (BSF) will also be introduced and discussed.

2.3.1. Ideal and non-ideal one-diode model

Figure 2.2a shows the basic model for an ideal PV cell. This model consists of a current source and a diode which are connected in parallel. The diode represents the PN junction. Therefore, the J-V characteristic of an illuminated PV cell that behaves as the ideal diode can be described by equation 2.4:

$$J(V) = J_0\left[exp\left(\frac{qV}{k_BT}\right)-1\right] - J_{ph} \tag{2.4}$$

where V is the applied voltage on the diode and J_0 is the saturation current density. The first term in equation 2.4 represents the dark diode current density while the second term represents the photo generated current density.

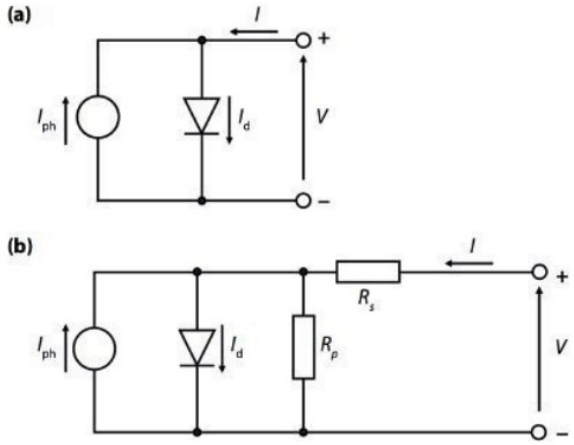

Figure 2.2: The equivalent circuit of (a) an ideal PV cell; and (b) a PV cell with series resistance R_s and shunt resistance R_p [3].

In practice, the FF of a PV cell is affected by two types of resistance: a series resistance (R_s) and a shunt resistance (R_p or R_{sh}). These resistances need to be included in the model as illustrated in Figure 2.2b. R_s encompasses the bulk resistance of the junction, the contact resistance between the junction and electrodes, and the resistance of the electrodes themselves. R_p, on the other hand, refers to the resistance caused by impurities and defects near the PN junction. Typically, it is desirable to keep R_s as low as possible to increase the amount of current that can be utilized in the external circuit. In contrast, R_p should be as high as possible to minimize leakage currents within the PV cell. The J-V characteristic of the non-ideal one-diode model is represented by equation 2.5.

$$J(V) = J_0\left[\exp\left(\frac{q(V-AJR_s)}{k_BT}\right)-1\right] + \frac{V-AJR_s}{R_p} - J_{ph} \tag{2.5}$$

where A is the area of the PV cell.

2.3.2. Non-ideal two diodes model

Due to additional recombination that occurs in the space charge region (SCR) of the PN junction, an additional saturation current density (J_{02}) has to be considered. This will reduce V_{oc} which will affect FF eventually. To account for this, the non-ideal diode has to be replaced by two diodes, an ideal one

that has an ideality factor equal to one and a non-ideal diode with an ideality factor higher than one. The new, more accurate two-diode model is illustrated in Figure 2.3.

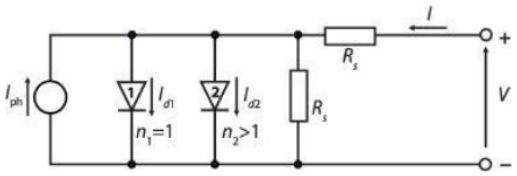

Figure 2.3: The equivalent circuit of a PV cell with two-diode model [3].

Furthermore, the J-V characteristic of the two-diode model can be described by equation 2.6:

$$J(V) = J_{01}\left[\exp\left(\frac{q(V - AJR_s)}{n_1 k_B T}\right) - 1\right] + J_{02}\left[\exp\left(\frac{q(V - AJR_s)}{n_2 k_B T}\right) - 1\right] + \frac{V - AJR_s}{R_p} - J_{ph} \quad (2.6)$$

where J_{01} and J_{02} represent the saturation current densities of the diodes, and n_1 and n_2 represent the ideality factors of the diodes.

2.3.3. Low-high junction

In addition to the discussed cell components earlier, another component sill has to be added, namely the low-high (LH) junction. This LH junction is usually ignored in the equivalent circuit of a PV cell since it has a negligible influence on the model, especially when only DC measurements are considered. However, In this work, it is essential to include it as both DC and AC measurements has to be executed. To understand how the LH junction is formed, Figure 2.4 will be used as an example. Figure 2.4 shows a schematic of a c-Si n^+-p-p^+ PV cell with a p^+ BSF and an Al back-contact. This cell consists of (from left to right) anti reflecting coating (ARC) to reduce the amount of reflected light and increase absorption, a phosphorus-doped n^+ emitter, a boron-doped p-type base, and an aluminuim-doped p^+ BSF, with Ag and Al metalized contacts at the front (connected to emitter) and back (conntected to base) surfaces, respectively [14]. The BSF helps to reduce the recombination of the electrons and holes by providing a strong electric field that pulls electrons away from the recombination centers and towards the electrodes. This helps to reduce the rate of recombination and increase the overall efficiency of the cell. The BSF is typically created by diffusing a p-type material into the back surface of the cell, creating a region of high hole concentration that acts as a sink for holes [3].

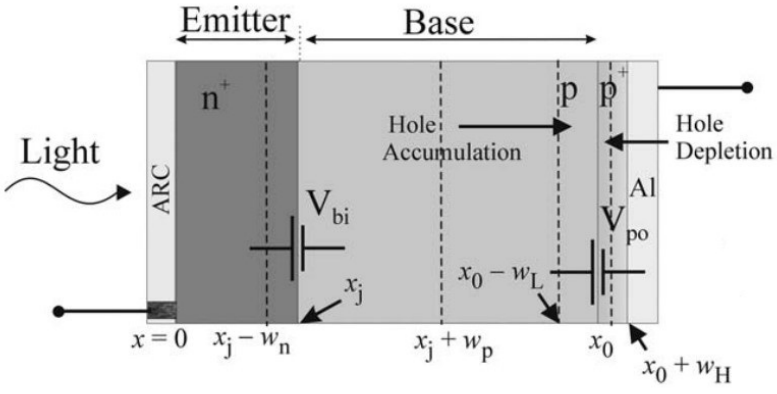

Figure 2.4: Schematic of a BSF c-Si PV cell [14].

Combining the emitter and base together will create a n^+-p junction which is located at x_j. The depletion region widths are w_n and w_p on the emitter and base sides, respectively. So, the total space

charge region (SCR) is $w_j = w_n + w_p$. In the depletion region a built-in voltage is formed and denoted with V_{bi}. Furthermore, the holes from the p^+ side of the LH interface (p-p^+ BSF) diffuse into the p side to form a hole-accumulation layer at x_0-$w_L \leq x \leq x_0$ and a hole-depletion layer at $x_0 \leq x \leq x_0$+w_H. This again forms a built-in voltage V_{p0} at x_0. Due to the electric field formed by the connection of LH-SCR, electrons from n^+-p junction will be repelled into the p-region. This will increase the cell efficiency and constitutes the main function of the BSF. Note that V_{bi} and V_{p0} have the same polarity which means that LH junction will be forward-biased when the PN junction is forward-biased [14]. By including the BSF (LH junction), the equivalent circuit for the PV cell will be as shown in Figure 2.5. Furthermore, It is important to note that this model is valid for all types of PV cells.

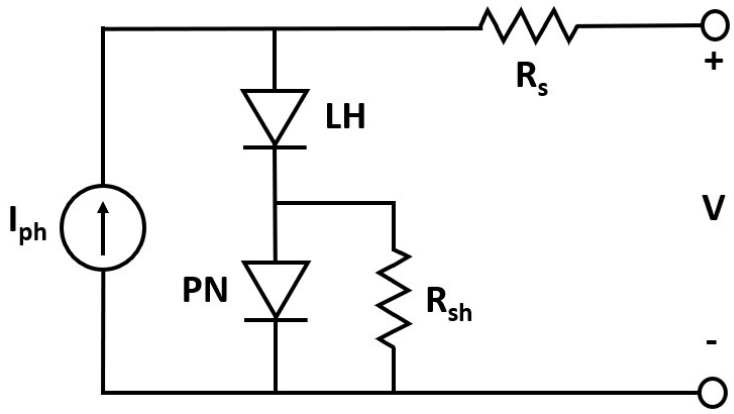

Figure 2.5: Equivalent circuit of a PV cell with LH junction.

2.4. Equivalent circuit of PV cell in AC mode

Up until now, the discussion has only focused on the direct current (DC) properties of the PN junction in a PV cell. However, when the PN junction is connected to an amplifier circuit that applies a sinusoidal signal superimposed on the DC current and voltage, the small-signal characteristics of the PN junction become important and must be considered in the equivalent circuit. This section will introduce and explain three small-signal components, which are the diffusion resistance R_d, the junction capacitance (or depletion capacitance) C_{dep}, and the diffusion capacitance C_{diff}. Finally, an equivalent circuit will be developed that illustrates the electrical behavior of the PN junction when small signals are applied. Note that many of the information in this section was taken from the book Semiconductor Physics and Devices written by Donald A. Neamen [15].

2.4.1. Diffusion resistance

Figure 2.6 shows the I-V characteristic of an ideal diode. This plot is obtained from equation 2.7:

$$I_D = I_s \left[\exp\left(\frac{qV_a}{k_B T}\right) - 1 \right] \tag{2.7}$$

where I_D is the current diode and I_s is the reversed-saturation current of the diode and V_a is the applied bias voltage.

By applying a DC voltage V_0 on a diode in forward bias, the diode will produce a DC diode current equal to I_Q. Then, a small sinusoidal voltage is applied by superimposing it with V_0. Therefore, a small sinusoidal current will be produced. By taking the ratio between the sinusoidal current dI_D and sinusoidal voltage dV_a, the incremental conductance g_d can be calculated as is shown in equation 2.8:

$$g_d = \frac{dI_D}{dV_a}\Big|_{V_a = V_0} \tag{2.8}$$

Therefore, g_d is equal to the slope ($= \frac{1}{R_d}$) as is shown in Figure 2.6. This means that R_d can be calculated using equation 2.9:

$$R_d = \frac{dV_a}{dI_D}\Big|_{I_D = I_{DQ}} \tag{2.9}$$

where R_d is the small-signal diffusion resistance and I_{DQ} is the DC quiescent diode current. From equations 2.7 and 2.9 it can be concluded that by increasing the bias voltage, R_d will decrease since the slope of the curve increases. On the other hand, in reverse-bias I_D will decrease and R_d will increase.

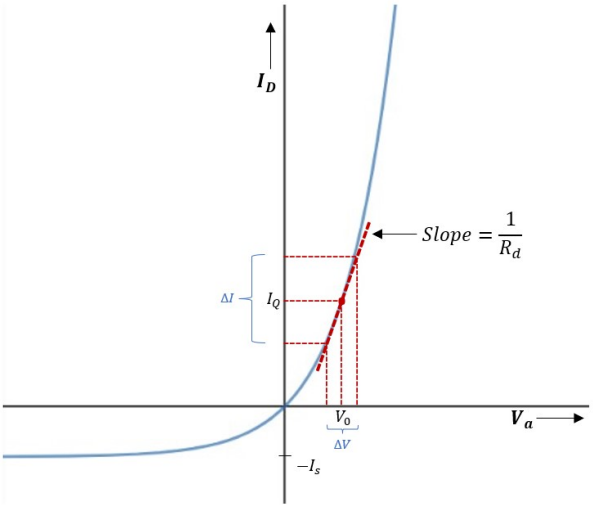

Figure 2.6: I-V curve of an ideal diode

2.4.2. Junction capacitance

When the p-type and n-type semiconductor materials are connected together, there will be a difference in electron concentration between n- and p-type regions. This encourages the electrons to move from the n-type to p-type region which will cause a diffusion current. Similarly, the holes in the p-type will move to the n-type region. After some time, the internal electrical forces will compensate the diffusion and this process will stop and a so called space charge region (or depletion region) will be formed as can be seen in Figure 2.7.

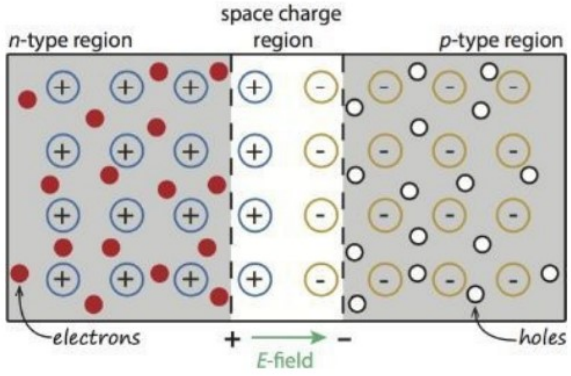

Figure 2.7: Connecting n- and p-type together and formation of the depletion region [3].

Due to the depletion region and the separation of electrons and holes, a capacitance will be formed in the PN junction. The charge densities in the depletion region can be seen in Figure 2.8. Note that Figure 2.8 is flipped horizontally (p-type on left and n-type on right) compared to Figure 2.7. Figure 2.8 shows how the depletion region will change by applying a reverse bias voltage V_R and by increasing it to V_R+dV_R. This is shown at the additional areas denoted with +dQ' in n region (width = dx_n) and -dQ' in p region (width = dx_p). The junction capacitance can be defined as:

$$C_{dep} = \frac{dQ'}{dV_R} \tag{2.10}$$

where

$$dQ' = qN_d dx_n = qN_a dx_p \tag{2.11}$$

N_d and N_a are the concentration of donor and acceptor atoms per cm^3, respectively. The unit of dQ' is C/cm^2, and that of the capacitance is F/cm^2.

Equation 2.12 descripes the width of the n-type region:

$$x_n = \sqrt{\frac{2\epsilon_s(V_{bi}+V_R)}{q}\left[\frac{N_a}{N_d}\right]\left[\frac{1}{N_a+N_d}\right]} \tag{2.12}$$

Filling equation 2.11 in 2.10 gives:

$$C_{dep} = \frac{dQ'}{dV_R} = qN_d\frac{dx_n}{dV_R} \tag{2.13}$$

Thus

$$C_{dep} = \sqrt{\frac{q\epsilon_s N_a N_d}{2(V_{bi}+V_R)(N_a+N_d)}} \tag{2.14}$$

Note that by considering that the space charge region is extended into the p region (x_p), the same equation for C_{dep} will be obtained.

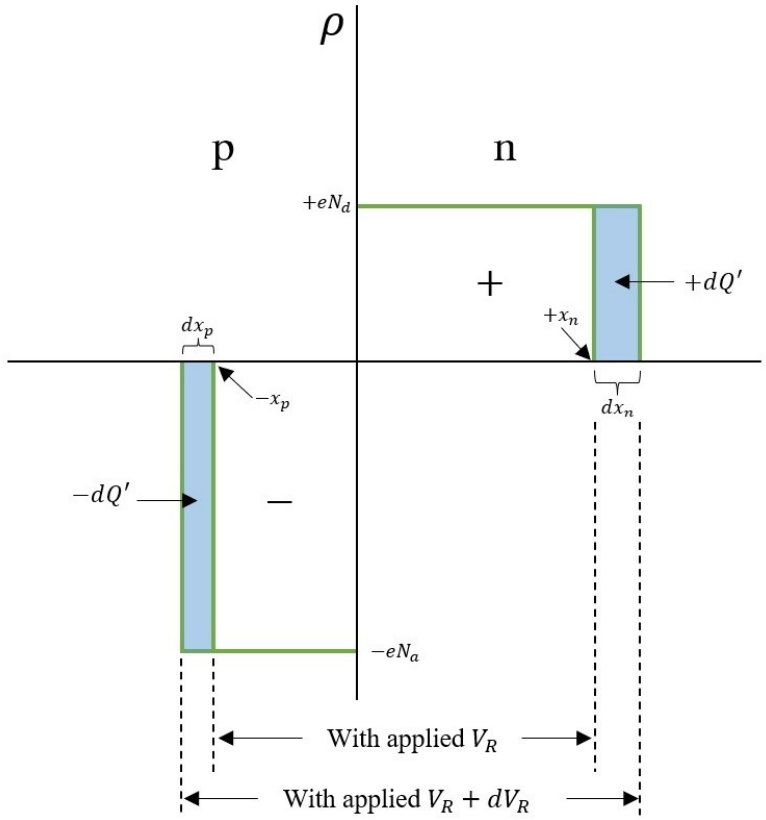

Figure 2.8: Differential change in the space charge width with a differential change in reverse-biased voltage for a uniformly doped PN junction.

2.4.3. Diffusion capacitance

When the PN junction diode is forward-biased, then the so called diffusion capacitance C_{diff} will play an important role. C_{diff} is formed due to the electrons and holes that diffuse from the n and p-type into the depletion region. To study this phenomenon, the PN junction diode is set at forward-biased using a DC voltage superimposed with a small AC voltage as is shown in Figure 2.9a. The total superimposed forward-biased voltage will be equal to $V_a = V_{dc} + \hat{v}\sin\omega t$.

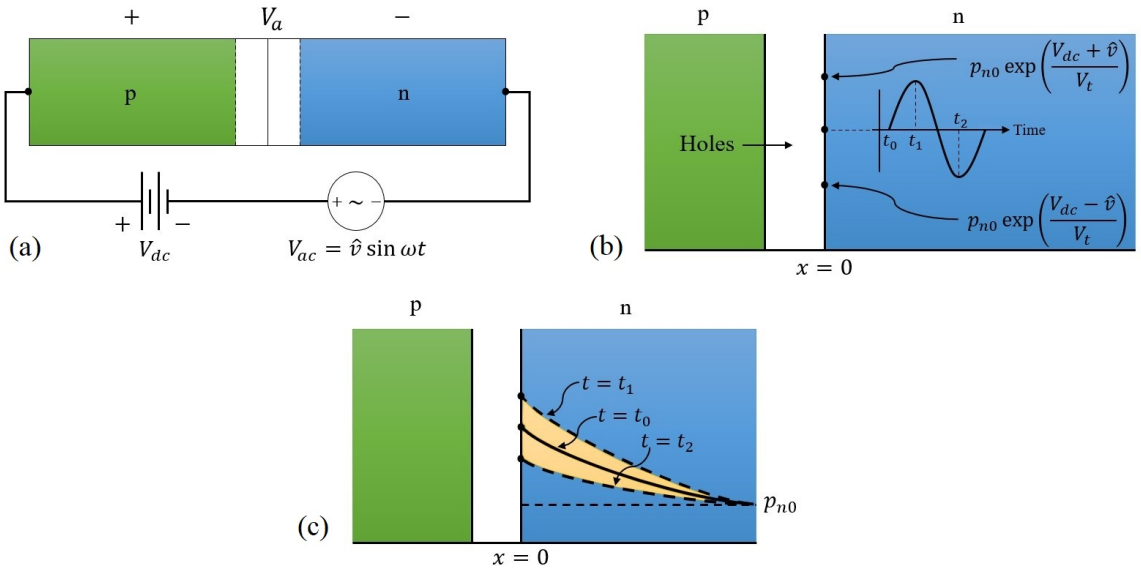

Figure 2.9: (a) A forward-biased PN junction using a DC voltage superimposed with an AC voltage; (b) the hole concentration as function of time at the space charge edge; (c) the hole concentration as function of distance in the n region at three different times.

Figure 2.9b shows the hole concentration at the edge of the depletion region as a function of time. At $t_0 = 0$, the AC voltage is zero and the hole concentration at $x = 0$ is expressed by $p_n(0) = p_{n0}\exp(V_{dc}/V_t)$ where $V_t = k_B T/q$. When the AC voltage increases and reaches its maximum at $t = t_1$, The hole concentration will also reach its maximum value. Similarly, the hole concentration will reach its minimum when the AC voltage decreases and reaches its minimum value. Furthermore, Figure 2.9c shows the hole concentration as a function of distance at $t = t_0$, t_1 and t_2. Assuming that the period of the AC voltage is large enough compared to the time needed for the holes to diffuse into the n region, the hole concentration as a function of distance can be treated as a steady-state distribution. So, the three black lines (two dashed and one solid) correspond to the hole distribution when the AC voltage is zero, maximum and minimum at $t = t_0$, t_1 and t_2, respectively. Moreover, the shaded yellow area represents the change in charge ΔQ occurring due to the charging and discharging process during one AC voltage period.

Similarly, this whole process occurs also in the p region as can be seen in Figure 2.10. It is important to note that C_{diff} is larger than C_{dep} at high forward-biased PN junction and can be expressed as follows:

$$C_{diff} = \frac{q^2 n_i^2}{2k_B T}\left(\frac{\sqrt{D_p\tau_{p0}}}{N_d} + \frac{\sqrt{D_n\tau_{n0}}}{N_a}\right)\exp\left(\frac{qV_F}{k_B T}\right) \tag{2.15}$$

where n_i is the intrinsic carrier concentration, V_F is the forward-bias voltage, D_p and D_n are the diffusion constants of holes and electrons, τ_{p0} and τ_{n0} are the lifetimes of holes and electrons, respectively. Note that equation 2.15 is only valid when $\omega\tau_{p0} << 1$ and $\omega\tau_{n0} << 1$, where ω is the radian frequency of the AC small signal.

Finally, the total capacitance of the PN junction is the summation of equations 2.14 and 2.15: $C_{tot} = C_{dep} + C_{diff}$. Keep in mind that C_{tot} is dominated by C_{dep} at reverse- and low forward-bias voltages. At high forward-bias voltages, C_{tot} is dominated by C_{diff}.

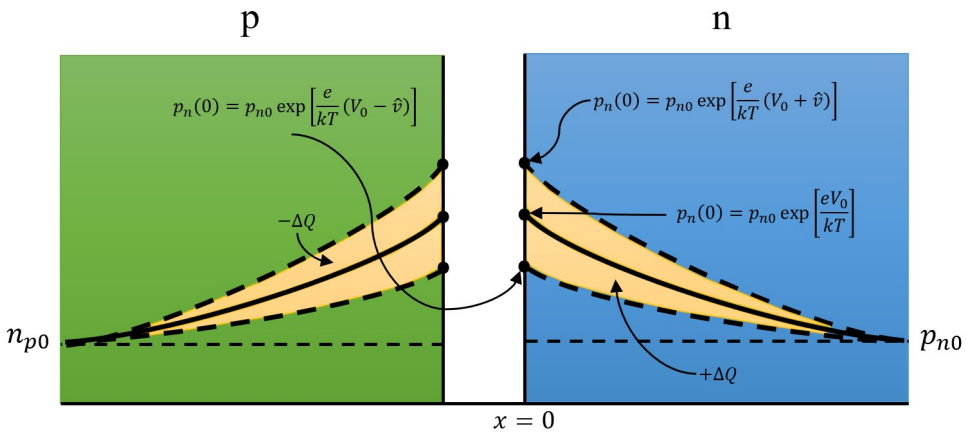

Figure 2.10: Minority carrier concentration changes with changing forward-bias voltage in n- and p-type regions.

2.4.4. Equivalent circuit of the small-signal model

As discussed earlier, the PN junction can be modelled using three components, namely, R_d, C_{dep} and C_{diff}. At high forward-biased PN junction, C_{dep} can be neglected and therefore the equivalent circuit will be drawn as in Figure 2.11a. However, the model should also represent the PN junction at reverse-bias and low forward-bias. Therefore, C_{dep} has been added to the model. This means that the two capacitances should be connected in parallel as depicted in Figure 2.11b.

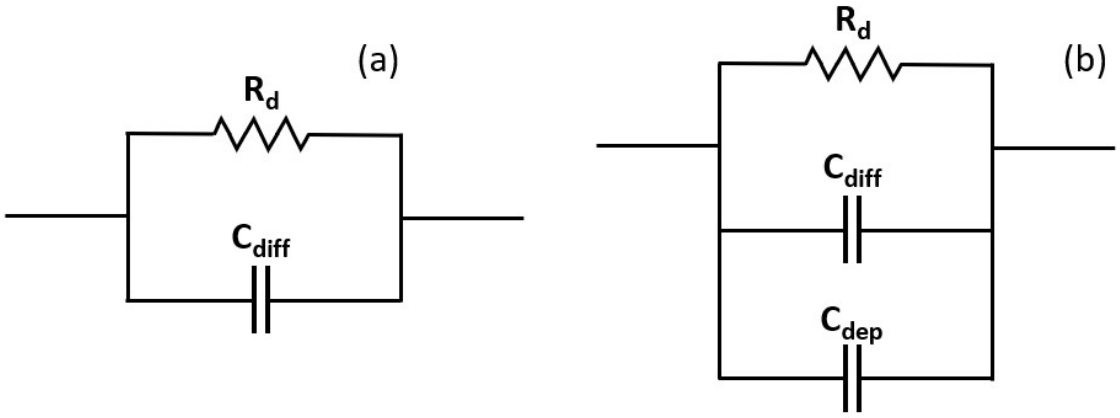

Figure 2.11: (a) Small-signal equivalent circuit of ideal forward-biased pn junction diode; (b) complete small-signal equivalent circuit of PN junction.

2.4.5. Equivalent circuit in AC mode

When a DC voltage is applied along with a small AC signal to the PV cell, it affects R_d, C_{dep}, and C_{diff}, as explained earlier. Consequently, it becomes necessary to employ the model depicted in Figure 2.11b to simulate the cell's behavior during AC measurements. By substituting the PN and LH diodes, as shown in Figure 2.5, with the small-signal model, the equivalent circuit can be represented as illustrated in Figure 2.12.

C_{dep} and C_{diff} can be combined together into $C_j = C_{dep} \parallel C_{diff}$. Similarly, R_d and R_{sh} can be combined into a single resistance, represented as $R_j = R_d \parallel R_{sh}$. Additionally, to account for the influence of series inductance L_s, particularly at high frequencies as noted in [14], an inductor is introduced into the circuit. Lastly, the series resistance of the PV cell, R_s, is included.

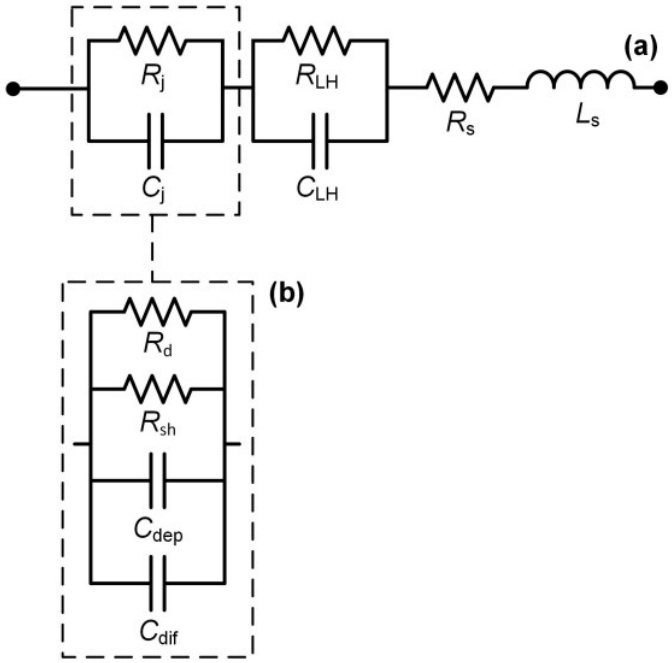

Figure 2.12: (a) Electrical equivalent model of a PV cell laminate that consists of R_j-C_j loop, R_{LH}-C_{LH} loop, R_s and L_s. (b) A detailed equivalent circuit that forms the R_j-C_j loop [16].

2.4.6. Circuit analysis of the PV cell

According to the final model shown in Figure 2.12, the total impedance of the PV cell can be expressed as follows:

$$Z_{PV} = R_s + j\omega L_s + \left[R_j || \frac{1}{j\omega C_j}\right] + \left[R_{LH} || \frac{1}{j\omega C_{LH}}\right] \tag{2.16}$$

Furthermore, equation 2.16 can be rewritten into the form $Z_{PV} = Z'_{PV} + jZ''_{PV}$ where Z'_{PV} is the resistance and Z''_{PV} is the reactance:

$$Z'_{PV} = R_s + \frac{R_j}{1+\omega^2 R_j^2 C_j^2} + \frac{R_{LH}}{1+\omega^2 R_{LH}^2 C_{LH}^2} \tag{2.17}$$

$$Z''_{PV} = \omega L_s - \frac{\omega R_j^2 C_j}{1+\omega^2 R_j^2 C_j^2} - \frac{\omega R_{LH}^2 C_{LH}}{1+\omega^2 R_{LH}^2 C_{LH}^2} \tag{2.18}$$

The complete derivation of these equations can be found in Appendix A. It is worth noting that the impedance of LH junction (Z_{LH}) will not be detected as long as the following conditions are satisfied: (i) $Z_j' \gg Z_{LH}''$, and (ii) $|Z_j'' \gg Z_{LH}''|$ [14]. These two conditions can be expressed as follows:

$$\frac{R_j}{1+\omega^2 R_j^2 C_j^2} >> \frac{R_{LH}}{1+\omega^2 R_{LH}^2 C_{LH}^2} \tag{2.19}$$

$$\frac{R_j^2 C_j}{1+\omega^2 R_j^2 C_j^2} >> \frac{R_{LH}^2 C_{LH}}{1+\omega^2 R_{LH}^2 C_{LH}^2} \tag{2.20}$$

Finally, in this projects, many experiments will be performed to measure the values of the circuit parameters: R_s, R_j, R_{LH}, C_j, C_{LH} and L_s at different DC operating points. Then, equation 2.17 and 2.18 will be used to fit the data to the measured values through complex nonlinear least-squares (CNLS) analysis. In the next chapter, the method of this thesis project will be introduced and more details about the use of CNLS and the setup of the experiment will be presented.

2.5. Constant phase element (CPE)

A constant phase element is a general model that can behave as a resistor, a capacitor or a combination of both. This component is commonly used to represent non-uniform dielectric properties such as interfaces, electrode coatings and porous materials. Furthermore, it can resolve electrochemical processes into faradaic and non-faradaic components [17]. Typically, CPE component is used to model the non-ideal characteristics of a capacitor. In the context of PV cells, these non-idealities stem from the presence of disordered junctions or systems that contain traps distributed across various energy levels and space, as described in [18]. Consequently, the capacitances within PV cells exhibit non-ideal behavior. Therefore, CPE is proposed in this work in order to improve the equivalent circuit model by considering the non-idealities of the PV cell. The CPE can be expressed as follows [17]:

$$Z_{\text{CPE}} = \frac{1}{Y_0(j\omega)^n} = \frac{cos(\frac{n\pi}{2}) - jsin(\frac{n\pi}{2})}{Y_0\omega^{-n}} \tag{2.21}$$

where ω is angular frequency, Y_0 is a constant representing the magnitude of the capacitance and n is the non-ideality parameter which determines the phase behavior. To understand the CPE component, an impedance plot is shown in Figure 2.13. The horizontal axis represents the real part of the impedance, while the vertical axis represents the imaginary part. When n = 0, the CPE behaves as an ideal resistor. On the other hand, if n = 1, then CPE behaves as an ideal capacitor with a phase shift of $\pi/2$. Finally, if $0 < n < 1$, then CPE behaves as a non-ideal capacitor which combines the properties of a resistor and capacitor together.

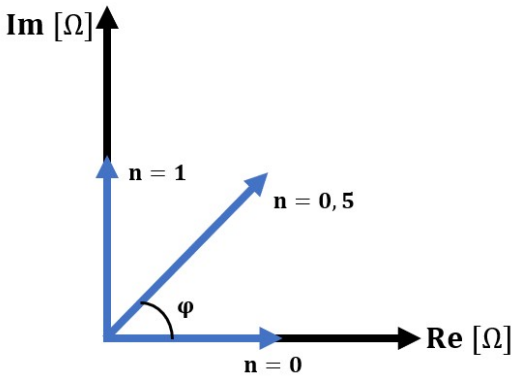

Figure 2.13: Impedance plot of CPE.

By replacing one of the capacitors with CPE, the equivalent circuit will be represented as shown in Figure 2.14. Following the same circuit analysis that has been done before, gives:

$$Z'_{PV} = R_s + \frac{R_2}{1+\omega^2R_2^2C_2^2} + \frac{R_1^2Y_0\omega^{-n}cos(\frac{n\pi}{2}) + R_1}{(R_1Y_0\omega^{-n} + cos(\frac{n\pi}{2}))^2 + sin^2((\frac{n\pi}{2})} \tag{2.22}$$

$$Z''_{PV} = \omega L_s - \frac{\omega R_2^2C_2}{1+\omega^2R_2^2C_2^2} - \frac{R_1^2Y_0\omega^{-n}sin(\frac{n\pi}{2})}{(R_1Y_0\omega^{-n} + cos(\frac{n\pi}{2}))^2 + sin^2((\frac{n\pi}{2})} \tag{2.23}$$

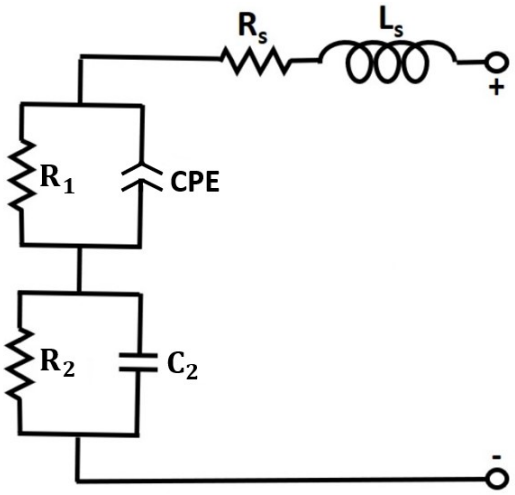

Figure 2.14: Simplified equivalent circuit with a CPE component under AC conditions.

3

Experimental method

In this chapter, the method and experimental setup that were used for this thesis are described. In section 3.1, the PV cells used for this study will be introduced and discussed. Then, the experimental setup will be shown and explained in details in section 3.2. Finally, the fitting procedure of the equivalent model will be presented and illustrated in section 3.3

3.1. Cell laminates used for this experiment

For this study, two single-cell laminates from distinct c-Si PV cell technologies, specifically IBC (Interdigitated Back Contact) and PERC (Passivation Emitter Rear Contact), were utilized as shown in Figure 3.1. Table 3.1 shows the corresponding laminated stacks for each cell. This table provides details on the materials and metallization structure employed in various laminates. The abbreviation "BB" represents busbar, "BC" indicates back-contacted, and "WBS" stands for a white backsheet from Icosolar PPF. The glass plates utilized are low Fe borosilicate glass without an anti-reflection coating. Commercially available EVA and TPO are used as encapsulants. To connect the cells to external setups, commercially available 0.2 mm × 0.5 cm Cu PV ribbons coated with eutectic SnBi solder are used.

Table 3.1: Materials and metallization structure used to laminate the PV cells.

	IBC	**PERC**
Mono (M)/Bifacial (B)	M	B
Cell area (cm2)	153	122.15
Front	glass	glass
Front encapsulant	EVA	TPO
Metal front side	-	9BB
Active layer	IBC	PERC
Metal back side	BC	9BB
Rear encapsulant	EVA	TPO
Back	WBS	glass

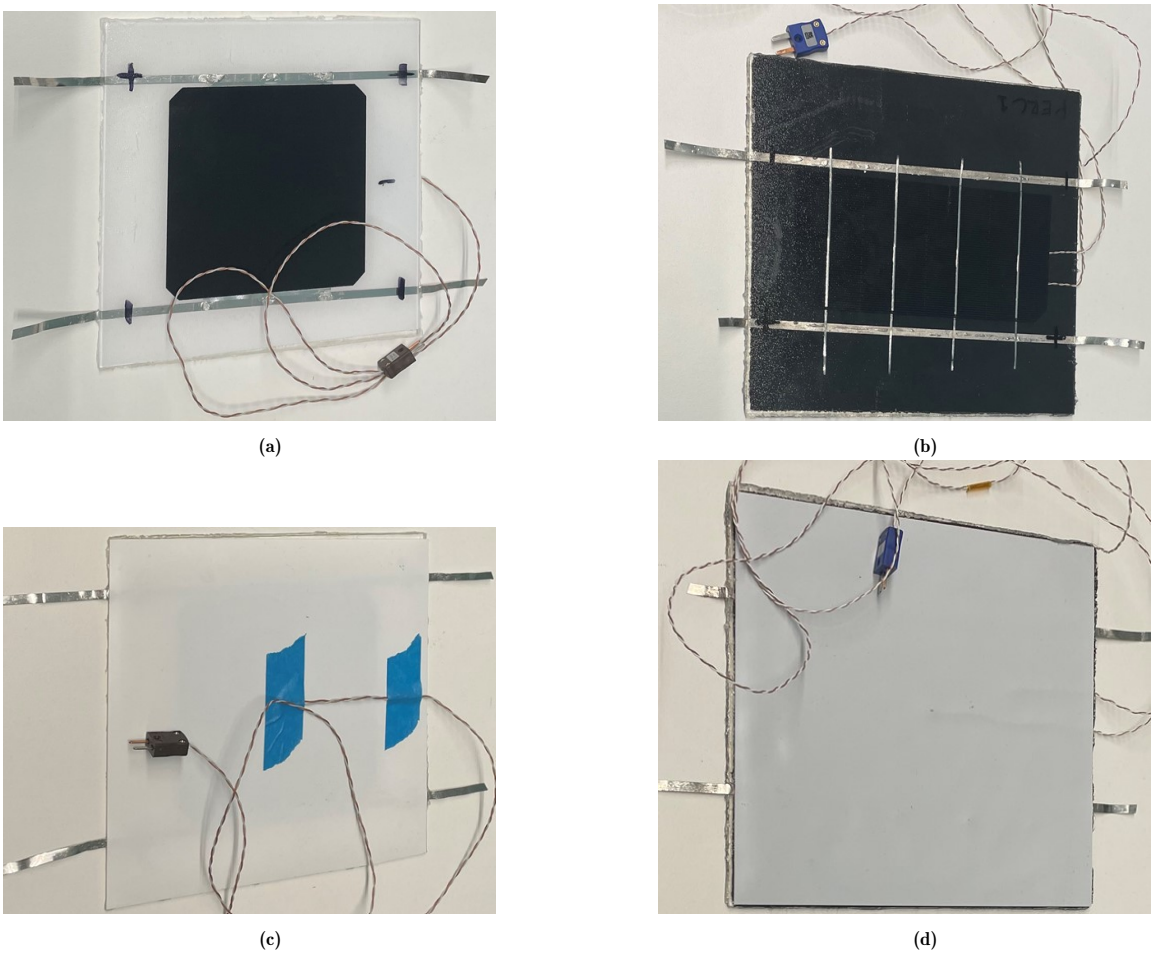

Figure 3.1: Photos of IBC and PERC cells used in this thesis project: (a) IBC cell laminate (front), (b) PERC cell laminate (front), (c) IBC cell laminate (back) and (d) PERC cell laminate (back).

Furthermore, the Enlite solar cell analysis system in the ESP lab at TU Delft was utilized to measure the J-V curves of the two single-cell laminates which are shown in Figures 3.2 and 3.3. These J-V curves were measured in STC and dark conditions and the corresponding STC parameters are presented in Table 3.2.

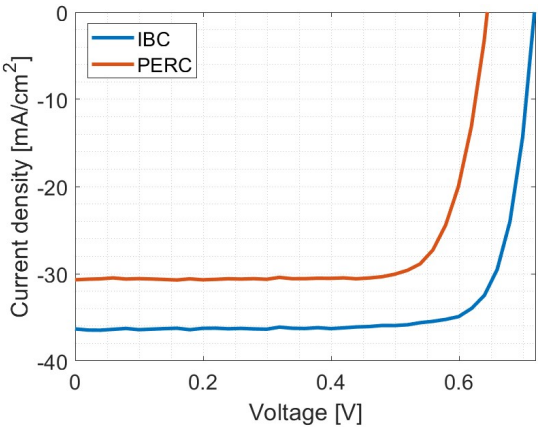

Figure 3.2: J-V curves of the single-cell laminates in STC conditions.

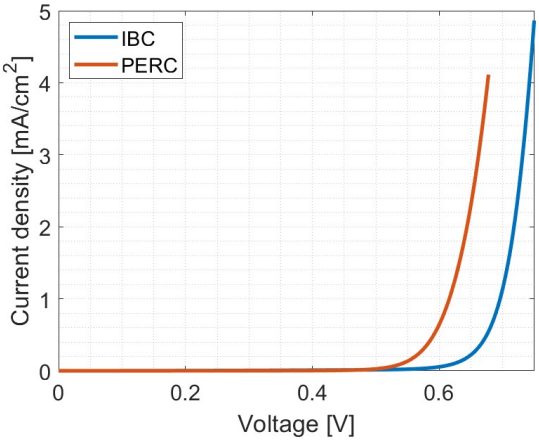

Figure 3.3: J-V curves of the single-cell laminates in dark conditions.

Table 3.2: STC parameters of the single-cell laminates investigated in this study, determined using the Enlite solar cell analysis system.

	IBC	**PERC**
Isc (A)	5.571	3.743
Voc (mV)	714.6	642.1
Impp (A)	5.17	3.49
Vmpp (mV)	619.5	539
Efficiency (%)	20.93	15.41
Fill Factor (%)	80.45	78.33
Jsc (mA/cm^2)	36.41	30.64
Rs (mΩ)	6.69	6.87

3.2. Impedance spectroscopy setup

The laminates employed in this study cannot be effectively characterized using conventional impedance spectroscopy setups. This is due to the fact that in dark conditions, the DC currents for the large-area cells surpass 0.5 A at DC bias voltages near 0.6 V. The commercial setups cannot operate within the necessary frequency range, which extends beyond 5 kHz, and are not equipped to analyze devices at high DC current and low DC voltage levels [16]. In order to evaluate the cells across a broad range of voltages, an impedance spectroscopy setup was developed in the Photovoltatronics Lab at the TU Delft. A diagram of this setup is depicted in Figure 3.4. In this setup, the Agilent 33250A function generator (FG) is used to establish the small-signal sinusoidal waveforms while a Keithley 2651A source measurement unit (SMU) is used to set the DC bias voltage (V_{DC}). The Keithley 2000 Multimeter is utilized to monitor the DC voltage of the PV cell. To combine V_{DC} with the sine wave signal, an OPA549 op-amp, configured as a non-inverting summing amplifier (IC1), is incorporated and powered by the EA-OS 2042-20 B power supply with 24V. Furthermore, this op-amp protects the function generator from high currents when the PV cell is operating under illumination. The 100kΩ resistors placed between the FG, SMU, and the positive input of the op-amp are employed to limit the current flowing through the op-amp. The additional 100kΩ resistors connected to the negative input of IC1 serve to maintain the gain of the op-amp at a value of 1. This ensures that the input signal applied to IC1 undergoes no amplification or attenuation before reaching the PV cell. The output of IC1 is connected to the positive contact of the PV cell. On the negative contact of the PV cell, another op-amp (IC2) is added and supplied by EA-OS 2042-20 B power supply with 24V to regulate the voltage at the negative contact of the cell. The 1Ω resistor positioned between the negative cell contact and the negative input of IC2 serves a stabilizing function within the circuit. Meanwhile, the second 1Ω resistor acts as a load. In this configuration, the op-amp replicates the voltage from the positive input to the negative input. At the positive input of IC2, a second power supply (PS2) was employed to set the value at the negative cell contact to 12V. This implies that when V_{DC} is adjusted to 12V, there is no voltage drop across the PV cell, and if V_{DC} is set to 12.5V, the voltage of the PV cell becomes 0.5V, and so on. The inclusion of IC2 in this configuration was driven by practical considerations. Without IC2, a bidirectional power supply would be required if the negative cell contact were directly connected to ground. Finally, it is important to highlight that when the PV cell is exposed to light, the current flows from the PV cell to the ground through IC1. Conversely, when the PV cell operates in the absence of light, the current flows to the ground through IC2.

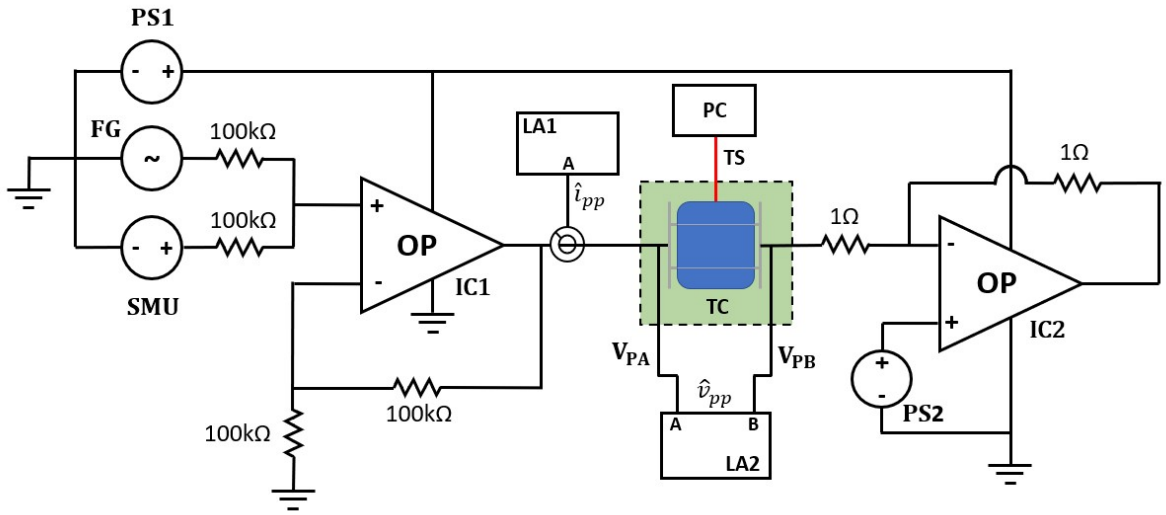

Figure 3.4: Overview of the in-house designed impedance spectroscopy setup. The power supplies 1 (PS1) and 2 (PS2) are both of the type EA-OS 2042-20, while the function generator (FG) is an Agilent 33250A. The opamp (OP) is of the type OPA-549 and is connected in non-inverting summing (IC1) and inverting (IC2) configurations. The source measurement unit (SMU) is used to set the bias voltage. The current probe (CP) is an Yokogawa 702916 connected to channel A of the EG&G Instruments 7260 DSP lock-in amplifier (LA1). Furthermore, the voltage probes (V_{PA}) and (V_{PB}) are connected to the positive and negative contacts of the PV cell, repectively. On the other side, V_{PA} and V_{PB} are connected to channel A and B of the Signal Recovery 7225 DSP lock-in amplifier (LA2). The temperature controller (TC) is of the type Thermo Scientific Polar Series Accel 500 LC. Finally, the temperature sensor (TS) is of the type RS pro type T used to measure the PV cell temperature which could be read by the computer (PC).

As one of the primary objectives of this study entails investigating the influence of temperature on PV cell impedance, a temperature control system with 80×80cm plate, namely the Thermo Scientific Polar Series Accel 500 LC, has been employed. This system facilitates controlled cooling and heating of the PV cell. Concurrently, a temperature sensor, specifically an RS pro type T thermocouple, has been utilized to monitor the cell's temperature dynamics. The sensor, characterized by a probe diameter of 1/0.2mm, can be directly affixed to the rear surface of the cell without causing any impairment during the lamination process. It is worth noting that this worked successfully only for PERC cell, whereas the IBC cell sustained damage during lamination. Consequently, the thermocouple was attached on the outside of a new laminate that do not include a thermocouple in the lamination stack as demonstrated in Figure 3.1c and 3.1d. To assess the accuracy of the sensor, an experiment was conducted, revealing a deviation of ±3°C. Importantly, the operational scope of this temperature sensor spans from -75°C to 250°C [19], which is suitable for the scope of this research. To read the temperature accurately, the sensor has been integrated with a computer (PC) and dedicated software has been employed to achieve this purpose. To investigate the influence of illumination on the PV cell, a white LED was employed for this purpose. Figure 3.5 shows the AM1.5 spectral irradiance (shown in blue) and the irradiance of the white LED at 1.7A and 28.4V (depicted in red) as a function of wavelength. It is worth noting that the right y-axis belongs to the LED spectrum with $\mu W/cm^2/nm$ as a unit, while the left y-axis represents the spectral irradiance and its unit is $W/m^2/nm$. Furthermore, it is observed that the white LED emits photons within the wavelength range of 350 to 850 nm, whereas solar irradiance covers a broader spectrum ranging from 300 to 2500 nm.

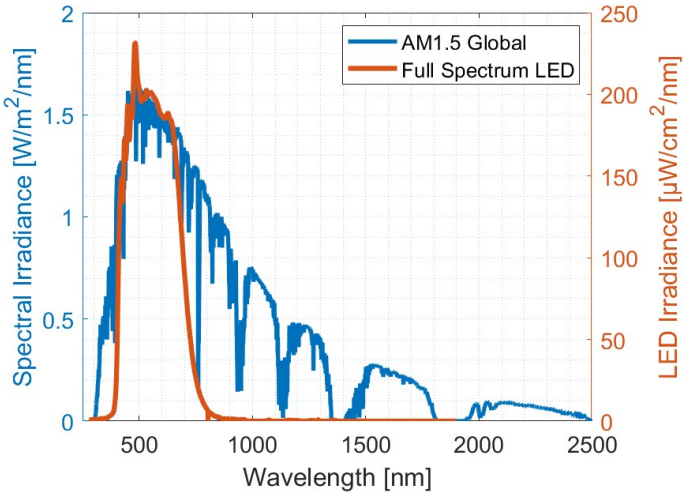

Figure 3.5: Spectral irradiance (blue) and white LED irradiance (red) as a function of wavelength.

To achieve precise and high-speed analysis of these signals, the impedance data presented in this manuscript are derived by analyzing the waveforms with lock-in amplifiers. The Yokogawa 702916 current probe (CP) is used to measure the sinusoidal current signal $\hat{i}$, which is linked to a EG&G Instruments 7260 DSP lock-in amplifier (LA1). Meanwhile, the Signal Recovery 7225 DSP lock-in amplifier (LA2) is used to record the sinusoidal voltage signal $\hat{v}$, where channel A's voltage probe is connected to the positive contact of the solar cell, and channel B's voltage probe is connected to the negative side. The A-B setting of the lock-in amplifier measures the difference between the two input voltages. Since the voltage and current signals are measured separately, parasitic cable effects are minimized in a manner comparable to four-terminal sensing [16]. The reference channel for both lock-in amplifiers is linked to the function generator, allowing for the extraction of the RMS amplitude and the phase shift of both $\hat{v}$ and $\hat{i}$ with respect to the function generator waveform.

The frequency-dependent impedance characteristics of PV cells were investigated within a frequency range spanning from 5 Hz to 120 kHz. The upper boundary of this range was determined by the maximum frequency capability of the 7260 DSP lock-in amplifier. Furthermore, an in-house developed LabView software was used to set the amplitude of $\hat{v}$, perform frequency sweeps with the function generator and record the measured values from the lock-in amplifiers. The level of automation implemented guarantees the reproducibility of experiments while mitigating the occurrence of human errors.
To obtain accurate and correct results, the applied sinusoidal signal $\hat{v}$ about a DC operating point should be sufficiently small to maintain the linearity of the response since solar cells are nonlinear devices [20, 21]. According to previous studies, $\hat{v}$ should be between 10 mV_{pp} and 28 mV_{pp} in order to execute impedance spectroscopy on c-Si PV cells and avoid nonlinearities [8, 14, 20, 21, 22, 23, 24]. It is important to mention that nonlinearities are expected to have a greater impact on measurements at DC bias points, where the I-V curve displays the most curvature [16]. According to [16], the excessive amplitude $\hat{v}_{pp}$ has a notable impact on the recorded impedance data. Nonlinearities at higher amplitudes result in an underestimation of impedance, a phenomenon that diminishes with increasing frequency. Nevertheless, maintaining a minimum amplitude is necessary to ensure a favorable signal-to-noise ratio during measurements for both $\hat{v}$ and $\hat{i}$. Particularly around zero bias on a PV cell with high shunt resistance, the current signal imposes limitations in this regard. In this study, the amplitude is adjusted based on the DC bias voltage, while $\hat{v}_{pp}$ is consistently kept below 1.5 mV_{pp} around the knee voltage of the I-V curve.

3.3. Fitting of the equivalent model

As discussed earlier, the impedance spectroscopy (IS) setup was used to obtain the impedance data. However, these data do not specify the values of the components of the equivalent circuit (shown in Figure 2.12). In order to do this, complex nonlinear least-squares (CNLS) analysis was used to fit the impedance data. CNLS is a method used to fit a mathematical model to a set of data points. The goal is to find the set of model parameters that minimize the difference between the observed data points and the values predicted by the model. The method uses an optimization algorithm to adjust the parameters until a best fit is achieved [25]. In this section, the method and CNLS algorithm will be introduced and explained. In Section 3.3.1, the fitting quality will be discussed. Then, Section 3.3.2 offers insights into the challenges and the fitting approach applied in this thesis work. Finally, the initial values and boundary conditions are described in Sections 3.3.3 and 3.3.4. It is important to note that many of the information in this section was taken from [16].

3.3.1. Evaluation of the fitting quality

In order to assess the fitting quality, two metrics were used in this study. The first metrics is the Root Mean Square Error (RMSE), which can be calculated using the following equation:

$$RMSE = \sqrt{\frac{\sum_{i=1}^{n}(X_{exp} - X_{model})^2}{n}} \tag{3.1}$$

where X_{exp} is the experimentally recorded data, X_{model} is the value that is predicted by the model with the best-fit circuit element values, and n represents the number of data points. The second metrics is Normalized Root Mean Square Error (NRMSE), which is calculated as follows:

$$NRMSE = \frac{RMSE}{X_{exp,max} - X_{exp,min}} \tag{3.2}$$

where $X_{\mathrm{exp,max}}$ and $X_{\mathrm{exp,min}}$ are the highest and lowest value of the experimentally recorded dataset, respectively. In this study, the fitting quality of impedance data is evaluated using both RMSE and NRMSE. These two metrics differ in how they scale or normalize the error, which makes them suitable for different purposes. For example, $\mathrm{NRMSE_M}$ is used for assessing the fitting quality of the magnitude, $\mathrm{NRMSE_R}$ for the real part of the impedance, and $\mathrm{NRMSE_X}$ for the complex part of the impedance. The purpose of normalization is to enable a fair comparison between impedance measurements obtained at different DC bias voltages. Notably, the magnitude of the impedance exhibits significant differences between low and high bias voltages. While the magnitude, resistance, and reactance are represented on linear scales, the phase is depicted on a periodic scale, which repeats after a certain value. As a result, RMSE_θ (Root Mean Square Error for the phase) was directly used without normalization to assess the fitting quality for the phase.

3.3.2. Challenges in fitting procedure and fitting approach

As previously discussed, Figure 2.12 illustrates the equivalent model that characterizes the dynamic behavior of the PV cell. This model is essential for fitting the impedance data gathered from the experimental setup. Nevertheless, it is imperative to address specific challenges and factors to enhance the optimization of the fitting process.

The first challenge to consider is the behavior of $\mathrm{R_{LH}}$-$\mathrm{C_{LH}}$ loop at varying $\mathrm{V_{DC}}$. According to [14], the $\mathrm{R_{LH}}$-$\mathrm{C_{LH}}$ loop remains undetected at low $\mathrm{V_{DC}}$ since the impedance of $\mathrm{R_{LH}}$-$\mathrm{C_{LH}}$ loop is insignificantly small compared to $\mathrm{R_j}$-$\mathrm{C_j}$ loop at such low voltages. Consequently, the impedance of the $\mathrm{R_j}$-$\mathrm{C_j}$ loop dominates the PV impedance, resulting in a Nyquist spectrum characterized by a semicircular shape. At higher $\mathrm{V_{DC}}$, the impedance of the $\mathrm{R_{LH}}$-$\mathrm{C_{LH}}$ loop becomes non-negligible which leads to a spectra that deviates from the semicircle [8].

The second challenge to consider is the impedance of $\mathrm{L_s}$. At low $\mathrm{V_{DC}}$, $\mathrm{L_s}$ has an insignificantly low impedance. This scenario could lead the solver to optimize the fit by essentially short-circuiting the inductor within the circuit leading to an overestimated $\mathrm{R_s}$ value. Therefore, $\mathrm{R_s}$ should not be fixed at a specific value; rather, it should be able to vary based on $\mathrm{V_{DC}}$. As a result, $\mathrm{R_s}$ lower and upper boundaries were applied and chosen to be $0.5 \times \mathrm{R_{s,Enlite}}$ and $2 \times \mathrm{R_{s,Enlite}}$, respectively, where $\mathrm{R_{s,Enlite}}$ is

the value obtained from the Enlite measurments. The determination of this range was predicated upon prior research concerning the dependency of R_s on V_{DC} [26]. On the other hand, L_s impedance becomes higher at higher V_{DC} leading to more realistic fitting values since it becomes less challenging to detect L_s.

The third challenge to consider is the voltages at which R_{LH}-C_{LH} loop becomes considerably high compared to R_j-C_j loop. The voltage ranges where this happens is between 300mV and 450mV depending on the type of PV cell, temperature and illumination level. This challenge is the most complex one and in order to solve it, some modifications in the model are required. This will be explained in more details in the next chapter.

In order to solve these challenges or reduce their impact and optimize the fitting, boundary conditions were introduced and applied. Both the initial values and the boundary conditions will be specified and explained in Section 3.3.3 and 3.3.4. Applying the boundary conditions could improve the fitting by avoid obtaining too low or too high values that have no physical validity. In this work, the fitting procedure goes as follows: at the beginning, a generalized PN fitting is performed which assumes that the equivalent circuit consists of only R_j-C_j loop, resulting in global fitting values. Indeed, this works properly for low V_{DC} values. For higher V_{DC}, the second stage of the fitting procedure, full model fitting, is activated. In this stage, the equivalent model will consist of both R_j-C_j and R_{LH}-C_{LH} loops. Furthermore, the global fitting values obtained by the first stage will be used as initial values in the second stage. Additionally, boundary conditions are applied in this stage to optimize the fitting.

Finally, to assess the most suitable model, both error metrics from Section 3.3.1 are employed. This process goes as follows:

1. the fitting values of PN fitting is only accepted if $NRMSE_M$, $NRMSE_R$, and $NRMSE_X$ are less than 0.015. Furthermore, the value of $RMSE_\theta$ should be lower than 2.5. In this case, only the values of R_j-C_j loop are documented. However, if any of these criteria are not met, the procedure advances to step 2.
2. The full model fitting will be used if one the previous conditions is not met. In this case, a comparison will be made between the full model fit and the PN fit. If the full model fit can achieve at least a 5% improvement in any of the previously unsatisfactory error metrics from step 1, the full model fit will be chosen. Otherwise, the PN fit is chosen.

The specific procedures employed for both PN fitting and full model fitting are outlined in Sections 3.3.3 and 3.3.4, respectively. As the optimal fit values obtained through CNLS analysis can be influenced by the initial parameter approximations, both the initial estimates and boundary conditions are provided.

3.3.3. Initial values of PN model

During the PN fitting process, the fit is conducted using the subsequent initial values:

- The initial value for R_j is adopted from the impedance data obtained by experimentation. Specifically, the magnitude recorded at the lowest frequency point within the characterization range is utilized. This magnitude represents the ratio between the amplitude of the voltage and current signals.
- The initial value for C_j is set at 10 μF.

3.3.4. Initial values and boundary conditions of full model

The full model fitting procedure is executed as follows:

1. Initially, a PN junction fit is conducted without considering the LH junction. The initial values for the parameters are set as follows:
    - Initial values for R_j and C_j remain consistent with those outlined in Section 3.3.3.
    - The initial value for R_s is adopted from the Enlite measurement presented in Table 3.2.
    - The initial value for L_s is set at 100 nH. The outcomes derived from this initial fit are subsequently denoted as $R_{s,init}$, $L_{s,init}$, $C_{j,init}$, and $R_{j,init}$.
2. Subsequently, a fitting process is executed employing all circuit elements illustrated in Figure 2.12. The initial values and boundary conditions are as summarized in Table 3.3:

Table 3.3: PV cell components with their initial values, lower and upper bounds.

PV cell component	Initial value	Lower bound	Upper bound
R_j	$R_{j,init}$	0	∞
C_j	$C_{j,init}$	0	∞
R_{LH}	$0.02\times R_{j,init}$	0	∞
C_{LH}	$0.2\times C_{j,init}$	0	∞
R_s	$R_{s,Enlite}$	$0.5\times R_{s,Enlite}$	$2\times R_{s,Enlite}$
L_s	100nH	0	∞

4

Results and discussion

In this chapter, the results obtained from the experiments will be presented and discussed. In Section 4.1, the Nyquist plots will be shown and analyzed. Then, the effect of temperature and illumination on the capacitive impedance of the PV cell will be discussed in Section 4.2. Finally, more results regarding the CPE model will be illustrated and studied in Section 4.3

4.1. Nyquist spectra

In this section, the Nyquist spectra of IBC and PERC cell laminates are studied and analyzed. In order to evaluate the values calculated by the CNLS algorithm, it is important to study the behavior and shape of the Nyquist plots. At the beginning, the Nyquist spectra at 30°C and in absence of light are considered as a reference and will be analyzed in Subsection 4.1.1. Then, in Subsection 4.1.2 the effect of temperature on the Nyquist spectra will be studied. Subsequently, the impact of illumination on the Nyquist spectra will be discussed in Subsection 4.1.3. Finally, the influence of both temperature and illumination at high frequencies and V_{DC} will be introduced and explained in Subsection 4.1.4.

4.1.1. Nyquist spectra in dark and at 30°C

Initially, in Figure 4.1, the Nyquist spectra of the IBC cell at 30°C and in absence of light are presented. These spectra were generated with applied V_{DC} ranging from 0mV to 650mV. The colored dots on the plot represent experimental data at various frequencies, while the black lines represent CNLS fits of this data based on the equivalent circuit illustrated in Figure 2.12. The data points start from the right side with the lowest applied frequency and extend to the left, forming a semi-circular shape as the highest frequency is reached. In the Nyquist plot, the $Z^{'}$-axis corresponds to the real part of the impedance, while the $Z^{''}$-axis corresponds to the imaginary part associated with the junction/trap capacitance and inductance [18].

For V_{DC} ranging from 0mV to 200mV (as shown in Figure 4.1a), the PN fitting model is employed because it provides sufficiently accurate fits. This model consists only of the R_j-C_j loop. This choice was verified by the error values presented in Table 4.1 as $NRMSE_M$, $NRMSE_R$, $NRMSE_X$ are below 0.015, and $RMSE_\theta$ is less than 2.5. In this particular range, the cell is weakly forward-biased, where $C_j \approx C_{dep} \gg C_{diff}$, and $R_j \approx R_{sh} \ll R_d$. There is (almost) no current ($J \approx 0$) flowing through the PN diode since the PN junction width is relatively high under low forward-bias. Thus, less charge carriers can diffuse between the n- and p-type semiconductor materials, resulting in relatively high potential barrier and impedance [3]. Furthermore, it is worth noting that the R_{LH}-C_{LH} loop has a minimal impact on the total impedance in low forward-bias [14]. In this region, one can deduce that equations 2.19 and 2.20 are satisfied.

By increasing the applied V_{DC}, it is noted that the radii of the Nyquist plots becomes smaller. At V_{DC} values of 300mV and 350mV (illustrated in Figure 4.1b), the full model fitting has been utilized to account for the R_{LH}-C_{LH} loop impedance. In this range, the curvature of the plots deviates from a semi-circular shape. This deviation is attributed to the R_{LH}-C_{LH} loop that appears and becomes

more prominent with increasing V_{DC}. It is important to note that equations 2.19 and 2.20 do not hold anymore since R_d decreases and C_{diff} increases when V_{DC} is increased.

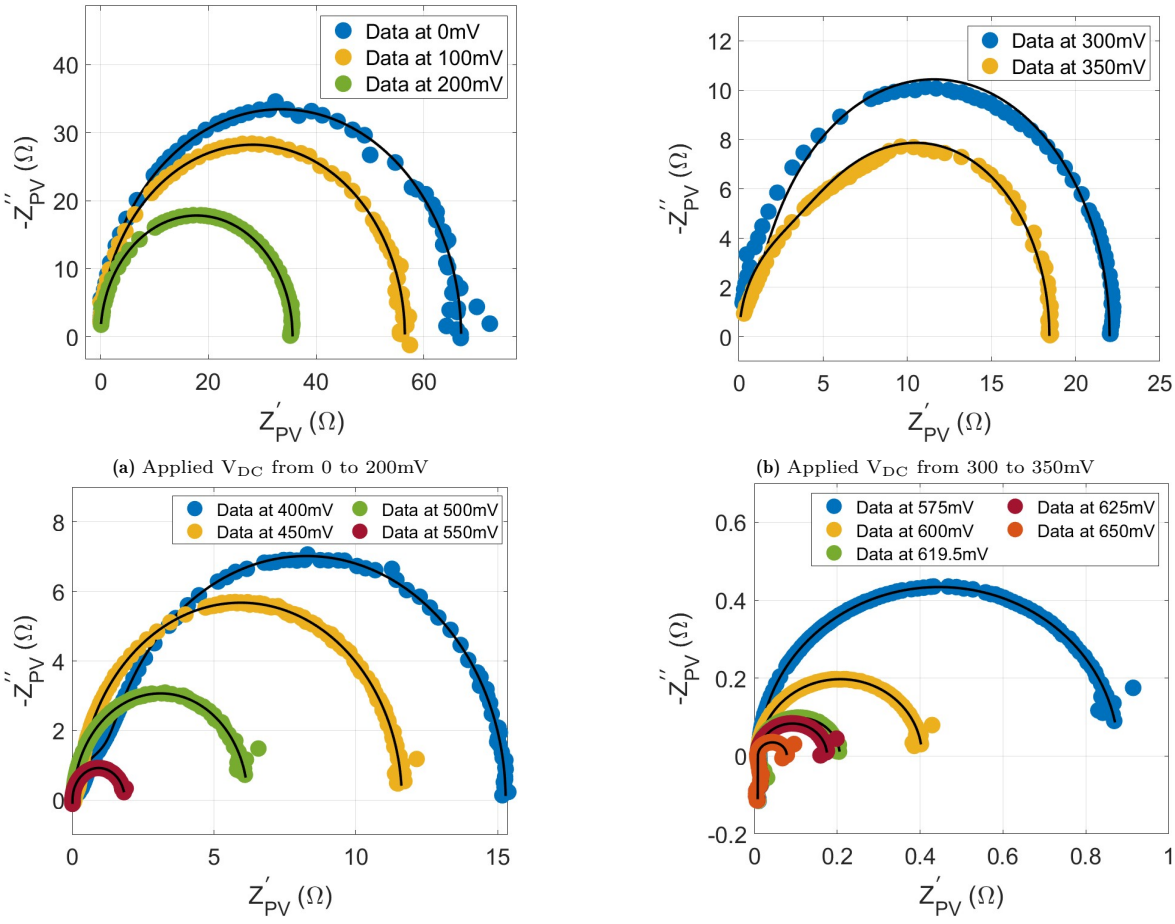

(a) Applied V_{DC} from 0 to 200mV

(b) Applied V_{DC} from 300 to 350mV

(c) Applied V_{DC} from 400 to 550mV

(d) Applied V_{DC} from 575 to 650mV

Figure 4.1: Nyquist spectra for the IBC cell laminate with V_{DC} gradually increasing from 0mV to 650mV at 30°C and in dark.

Furthermore, the performance of the equivalent model appears to be suboptimal in this voltage range and to a lesser extent at 400mV and 450mV. This observation is supported by the $RMSE_\theta$ values which are relatively high as shown in Table 4.1. This problem seems to be related to the value of R_s and its upper bound. By increasing the upper bound, the $RMSE_\theta$ values were lowered significantly since the model was more relaxed and able to reach the R_s value that was measured by the experimental setup as depicted in Figure 4.2. By increasing the upper bound at 450mV from $2\times R_{s,Enlite}$ to $10\times R_{s,Enlite}$, the $RMSE_\theta$ decreased to 1.702 while the other error values remain almost the same. This research was extended to investigate the voltage range in which this phenomenon occurs. The findings indicate that in the voltage range from 300 to 350mV, solely increasing the upper bound of R_s does not significantly improve the fitting. This is because, within this range, not only R_s but also the initial values and boundary conditions of the R_{LH}-C_{LH} loop play a crucial role in achieving a satisfactory fit. Furthermore, for V_{DC} values of 400, 450, and 500mV, it was observed that the upper bound of R_s had to be set at $30\times R_{s,Enlite}$, $10\times R_{s,Enlite}$ and $4\times R_{s,Enlite}$, respectively, in order to achieve a $RMSE_\theta$ value below 2.5. Additionally, it is important to mention that this phenomenon is exclusive to IBC cell, as PERC cell exhibit error values below the suggested threshold values outlined in Chapter 3. This leads to the conclusion that this phenomenon is closely associated with structural differences between the two types of PV cells.

Although relaxing the upper bound of Rs reduces the fitting error for IBC cell, it might lead to an overestimation compared to the actual series resistance of the PV cell. Therefore, it was decided to

keep the upper bound for R_s at $2\times R_{s,Enlite}$. In addition, the fit in Figure 4.2 still shows a small arc (in green) which is related to $R_{LH,init}$ and $C_{LH,init}$. However, this relation is more complex as the two initial values has to be chosen carefully in order to optimize the fitting even further.

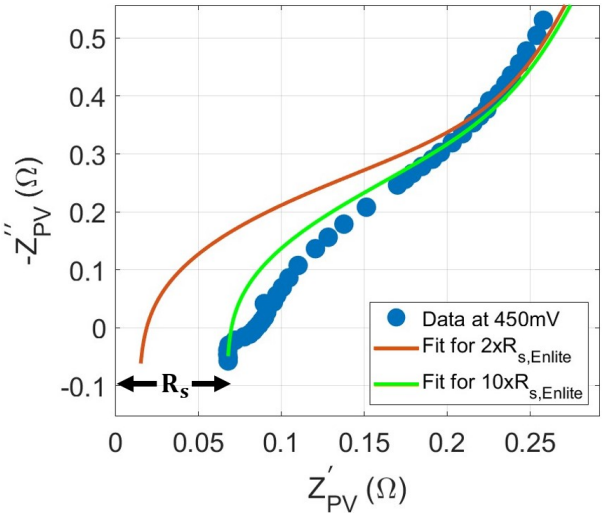

Figure 4.2: Nyquist spectrum for IBC cell at 450mV illustrating the effect of the series resistance on the fitting

At 300mV, the significance of the R_{LH}-C_{LH} loop becomes evident. However, this loop's size diminishes in comparison to the R_j-C_j loop as the V_{DC} values increase, as illustrated in Figure 4.1. When examining the Nyquist spectra presented in Figure 4.3a, the impact of the R_{LH}-C_{LH} loop may not be immediately apparent. Yet, upon closer inspection in the high-frequency range, this effect becomes more distinct. This effect is revealed better in Figure 4.3b, which displays the Nyquist spectra shape at V_{DC} = 450 and 500mV. The black arrows point to the regions of the R_{LH}-C_{LH} loop.

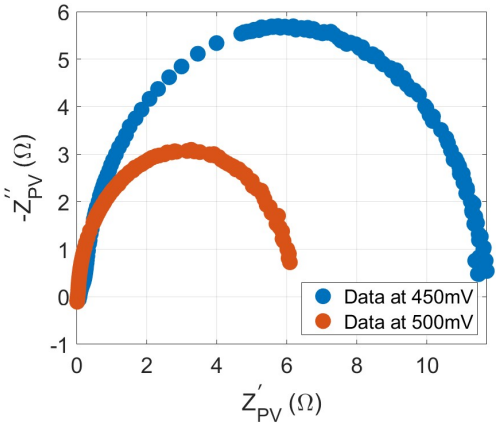

(a) Applied V_{DC} at 450 and 500mV

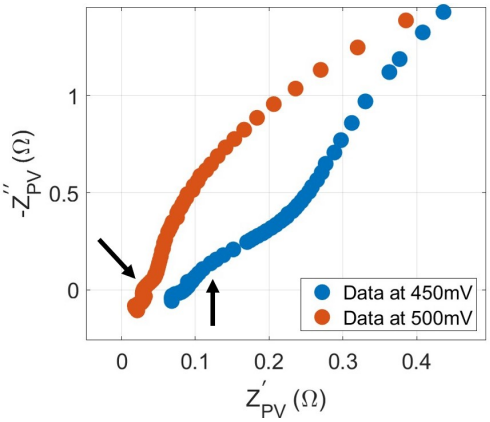

(b) Applied V_{DC} from 450 to 500mV (zoomed-in)

Figure 4.3: Nyquist spectra at 30°C and in dark at V_{DC} = 450 and 500mV.

By increasing V_{DC} further from 500 to 650 mV, C_j becomes totally dominated by C_{diff} ($C_j \approx C_{diff}$) and R_j by R_d ($R_j \approx R_d$). The R_j-C_j loop becomes more dominant even at higher frequencies. The size of R_j-C_j loop increases compared to the R_{LH}-C_{LH} loop as shown in Figure 4.4. Moreover, both loops go into the negative imaginary part region of $-Z_{PV}{}''$. This means that there is a change in phase from negative to positive due to the increase of the inductive reactance at such high frequencies and V_{DC} values. At these conditions, the impedance of both R-C loops decreases while the impedance of L_s increases. As stated by [14], the value of R_s is notably influenced by V_{DC}, which is also observed in Table 4.1. Figure 4.4 illustrates that $Z_{PV}{}'$ (including R_s) fluctuates both upward and downward at higher frequencies and V_{DC}. However, the used fitting model is insufficient to account for these

fluctuations. This phenomenon might be related, in part, to the influence of the experimental setup on the measured impedance. In other words, the measurement does not only represent the impedance of the PV cell, but might be influenced by the other connected components such as the opamps and cables. Furthermore, it was noticed that V_{DC} fluctuates by $\pm$ 0.5mV during the frequency sweep, which can lead to fluctuations in R_s and therefore overestimating its value. Another aspect to consider is the effect of the chosen model. Consequently, an alternative model will be presented and discussed in the following sections to evaluate its ability for improving the fitting accuracy. Finally, it is important to note that the Nyquist spectra (at 30°C and in absence of light) and best-fit values for PERC cell can be found in Appendix B.1. Furthermore, it is worth mentioning that there are some significant differences between the IBC and PERC cells. For example, the applied V_{DC} on PERC cell was only up to 550mV as it has a lower V_{oc} than that of IBC. Also, the R_{LH}-C_{LH} loop starts to appear at different V_{DC} ranges. However, the same explanation used for IBC cell holds for PERC taking into account the different V_{DC} ranges.

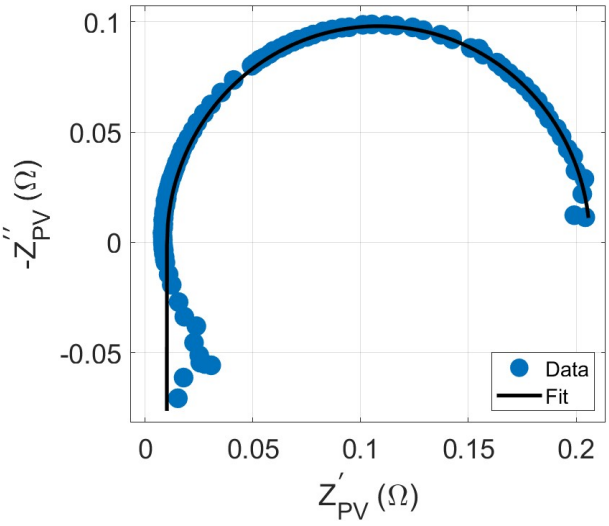

Figure 4.4: Nyquist spectrum at 619.5mV and 30°C in dark illustrating the effect of high V_{DC} (close to V_{oc}) on the fitting

Table 4.1: Best-fit values for the IBC cell laminate in dark and at 30°C.

V_{DC} (mV)	C_j (μF)	R_j (Ω)	C_{LH} (μF)	R_{LH} (mΩ)	R_s (mΩ)	L (nH)	$NRMSE_M$ (-)	$RMSE_\theta$ (-)	$NRMSE_R$ (-)	$NRMSE_X$ (-)
0	0.57	66.88	-	-	-	-	0.0138	0.8418	0.0132	0.018
100	0.63	56.45	-	-	-	-	0.0061	0.8133	0.0059	0.0126
200	0.71	35.62	-	-	-	-	0.0048	0.6061	0.0045	0.0062
300	1.195	20.74	1.119	1275.2	3.345	75.3	0.0140	5.1221	0.0158	0.0315
350	4.391	14.65	2.392	3782.7	8.233	64.6	0.0100	4.5390	0.0137	0.0235
400	18.60	13.95	7.756	1338.8	13.38	108.2	0.0050	9.9276	0.0065	0.0095
450	101.2	11.35	57.26	259.5	13.38	129.5	0.0056	11.589	0.0053	0.0127
500	550.9	6.134	400.2	40.3	13.38	145.7	0.0076	4.6069	0.0064	0.0206
550	2119	1.843	119.1	6.411	10.32	150.7	0.0128	1.7915	0.0042	0.0234
575	3694	0.867	50.01	3.036	8.819	147.7	0.0057	1.7942	0.0049	0.0123
600	6119	0.395	90.00	0.005	9.894	147.2	0.0077	2.7127	0.0071	0.0135
619.5	9199	0.196	8.792	0.033	10.11	101.5	0.0162	7.0072	0.0222	0.0161
625	10174	0.167	29.23	0.558	8.118	147.4	0.0144	3.3980	0.0143	0.0156
650	16771	0.070	1.606	0.405	7.792	147.1	0.0127	3.9205	0.0243	0.0087

4.1.2. Effect of temperature on Nyquist spectra

To examine how temperature impacts the PV cell impedance, it is crucial to understand the underlying theory. When the temperature increases, the Fermi-Dirac distribution function will increase meaning that electrons will be able to occupy more energy states and be more distributed [3]. Furthermore, the intrinsic carrier concentration (n_i) will increase as described in the following equation [27]:

$$n_i = \alpha T^{3/2} \exp\left(\frac{-E_g}{2k_b T}\right) \tag{4.1}$$

where α is a constant that depends on the effective masses of electrons and holes in the conduction and valence bands of Si, respectively and E_g, the bandgap of the semiconductor material which has a negligible temperature dependence [27]. In addition, the increase in n_i results in an increase in the saturation current (J_0) according to the following equation [3]:

$$J_0 = q n_i^2 \left(\frac{D_n}{L_n N_a} + \frac{D_p}{L_p N_d}\right) \tag{4.2}$$

where q is elementary charge, D_n and D_p are diffusion coefficients for n and p-type semiconductor materials, respectively. Furthermore, L_n and L_p are the electron and hole diffusion lengths, respectively. Finally, N_a and N_d are the concentration of acceptor and donor atoms per cm^3, respectively. In conclusion, at higher temperatures, n_i increases which results in a higher J_0. This will decrease V_{oc} according to the relationship described in equation 2.1.

Figure 4.5 shows three Nyquist spectra for the IBC cell in absence of light, at V_{DC} = 619.5mV (maximum power point voltage at STC for IBC) and T = 30, 45, 60°C. From this figure, it is observed that the diameter of the semicircle decreases once the temperature is increased. In other words, the sum of R_j + R_{LH} + R_s decreases. Furthermore, increasing the temperature leads to a smaller arc. To understand this behavior, it is important to start with the I-V curves corresponded to these three temperatures. From Figure 4.6a, it can be concluded that the I-V curve shifts to the left with increasing temperatures. This shift is due to the increase in n_i which results in a higher current as discussed earlier. As an effect of this increase, the impedance of the cell decreases. It is important to note that the diameter of the Nyquist spectrum corresponds to the slope of the I-V curve. To verify this, one can calculate the decrease in impedance using R = dV/dI and the values shown in Figure 4.6b. This gives the following results: $R_{30°C} \approx 0.20\Omega$, $R_{45°C} \approx 0.088\Omega$ and $R_{60°C} \approx 0.041\Omega$. Additionally, The Nyquist spectra start at $Z'_{PV,30°C} = 0.204\Omega$, $Z'_{PV,45°C} = 0.095\Omega$ and $Z'_{PV,60°C} = 0.047\Omega$ which represent R_s + R_j + R_{LH} at low frequency. Dividing $R_{30°C}/R_{45°C}$ and $R_{45°C}/R_{60°C}$ yields reduction fractions of 2.3 and 2.15, respectively. Similarly, applying this approach to $Z'_{PV,30°C}/Z'_{PV,45°C}$ and $Z'_{PV,45°C}/Z'_{PV,60°C}$ results in reduction fractions of 2.15 and 2.02. Upon comparing these ratios, slight discrepancies of around 0.15 and 0.13 become evident. These disparities could be related to the following factors: firstly, althought $Z'_{PV} \approx R_s + R_j + R_{LH}$, the other components, namely C_j and C_{LH} still have a relatively small effect even at low frequency according to equation 2.17. Secondly, since the experimental setup was responsible for the Nyquist spectra, while the I-V curves were measured using a different device, this could lead to variations attributed to measurement errors.

Finally, this explanation also holds for PERC cell despite the deviations in cell area, impedance values and V_{DC} ranges. The Nyquist spectra and I-V curves for PERC cell can be found in Appendix B.2. It is important to note that fitting the data for both cells becomes more difficult at higher temperatures as shown in Figure 4.5 and B.2 due to the reasons that have been discussed earlier.

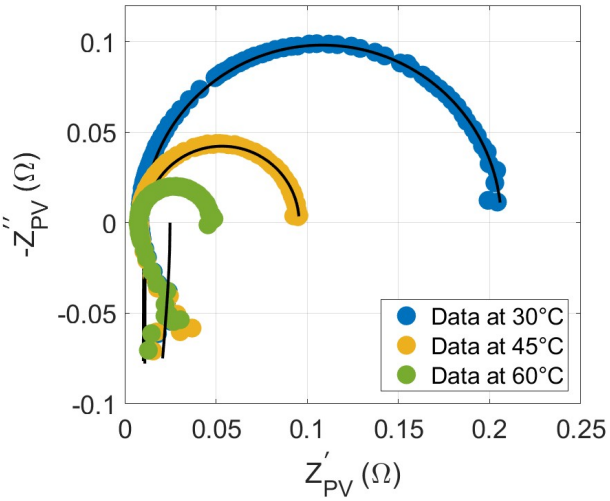

Figure 4.5: Nyquist spectra of IBC cell in dark, at 619.5mV and different temperatures.

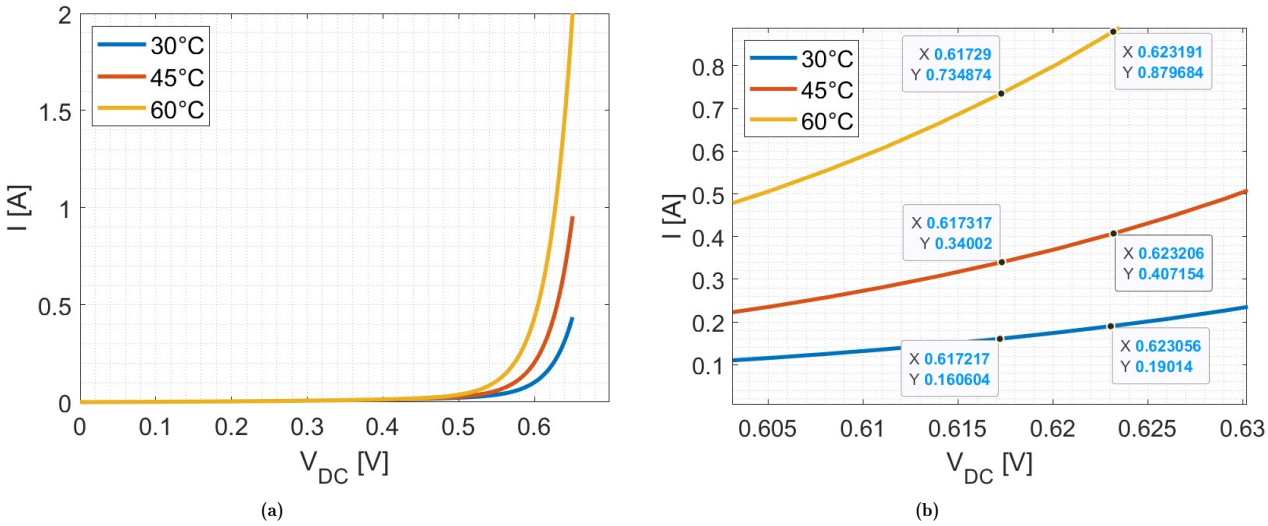

(a) (b)

Figure 4.6: (a) I-V curves of IBC cell in dark, at V_{DC} = 619.5mV and T = 30, 45, 60°C and (b) I-V curves (zoomed-in).

4.1.3. Effect of illumination on Nyquist spectra

Such as temperature, light intensity can also affect the PV cell impedance. To illustrate this, three Nyquist spectra are plotted for the IBC cell at T = 30°C, V_{DC} = 200mV and different light intensities as shown in Figure 4.7. From this figure, it is observed that the radii of the semi-circular shape becomes smaller and the curvature of the Nyquist spectrum deviates from the semi-circular shape when the light intensity is increased. Thus, the impedance decreases as the intensity is increased. This is mainly related to the effective voltage drop over the PN junction which becomes higher than V_{DC} as the cell is illuminated. The decrease in impedance can also be verified using the I-V curves shown in Figure 4.8. By applying the same approach used before at 200mV, the following ratios were obtained: R_{dark}/R_{250} and R_{250}/R_{500} yields reduction fractions of 1.26 and 1.24, respectively. Similarly, applying this approach to $Z'_{PV,dark}/Z'_{PV,250}$ and $Z'_{PV,250}/Z'_{PV,500}$ results in reduction fractions of 1.26 and 1.23. It is worth noting that at higher light intensity, the R_{LH}-C_{LH} loop becomes more prominent even at low V_{DC} (200mV in this case). When the PV cell is illuminated, $R_{sh} \approx R_j$ becomes smaller at low forward bias voltages. This was verified by calculating R_{sh} around 0V using the I-V curves. Consequently, the R_{LH}-C_{LH} will be detectable at lower voltages compared to dark measurements.

Another aspect to consider is the fitting of the data. In the voltage ranges where the LH junction impedance is relatively high compared to the PN junction impedance, the fitting encounters challenges to find the optimal values. These challenges are related to the chosen boundary conditions and initial values which have to be adjusted manually to obtain better fitting values. Finally, to examine the illumination effect on PERC cell, three Nyquist spectra were plotted as shown in appendix B.3. In contrast to IBC cell, the fitting model does not encounter any problem to fit the data of the PERC cell. However, it is obvious that the data of PERC cell under illumination contains more noise, especially at low frequencies. This noise could be related to the relatively high impedance of PERC cell compared to IBC. In other words, the same applied sinusoidal signal $\hat{v}_{pp}$ on both cells results in a smaller $\hat{i}_{pp}$ for PERC cell.

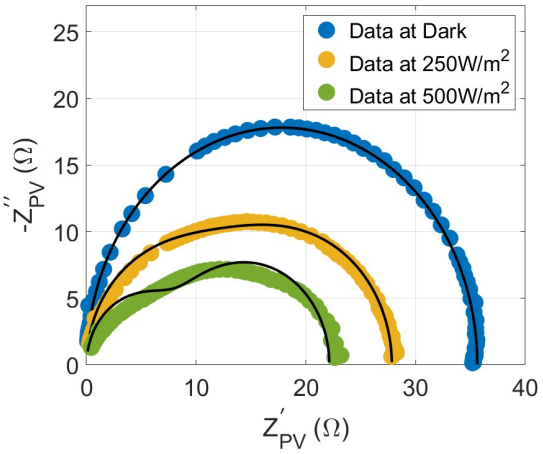

Figure 4.7: Nyquist spectra of IBC cell at V_{DC} = 200mV, T = 30°C and intensity = 0, 250 and 500W/m^2.

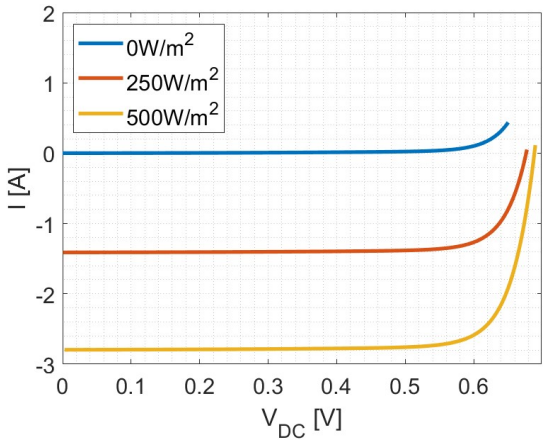

Figure 4.8: I-V curves of IBC cell at 30°C and intensity = 0, 250 and 500W/m^2.

4.1.4. Effect of temperature and illumination at high frequency and DC voltages

As illustrated in Figures 4.4 and 4.5, the gathered data exhibit an unusual trend at higher frequencies and V_{DC}. To investigate this phenomenon, Nyquist spectra for both cell laminates were plotted at V_{DC} = 619.5 and 539mV (maximum power point voltages at STC for IBC and PERC, respectively), various temperatures and illumination levels, as demonstrated in Figures 4.9 and 4.10.

Firstly, the effect of temperature was explored. This entailed collecting data in the absence of light and at temperatures of 30, 45, and 60°C. As illustrated in Figure 4.9a, the temperature's impact in this range was found to be limited. Conversely, Figure 4.9b demonstrates a clear shift in impedance for the PERC cell. Furthermore, it is important to note that the high frequency impedance data for the IBC cell are closer to each other around $Z''_{PV} = 0\Omega$, unlike the PERC cell. However, this discrepancy is linked to V_{DC}, as other IBC data (at V_{DC} = 500mV) also displayed variations in Z'_{PV} values at $Z''_{PV} = 0\Omega$. Altering the V_{DC} leads to a different R_s value, consequently causing a distinct position along the Z'_{PV}-axis.

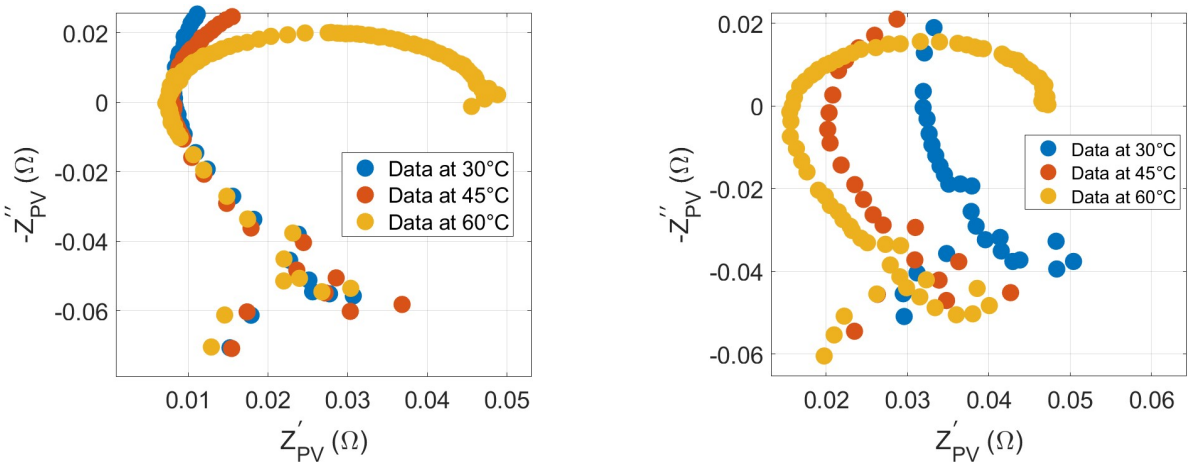

(a) IBC (b) PERC

Figure 4.9: Nyquist spectra of IBC and PERC cells in dark, at V_{DC} = 619.5 and 539mV, respectively and T = 30, 45, 60°C (zoomed-in).

To investigate the impact of illumination at high voltages and frequencies, Figure 4.10 has been generated. From this figure, it is observed that the level of illumination shows a notable effect on the impedance behavior. For both types of cell laminates, the fluctuations in impedance decrease and the data exhibit greater stability as the illumination level increases. The reason behind this increased stability is still unclear yet. However, it is suspected that increasing the illumination decreases the fluctuations in V_{DC} which results in a more stable R_s at high frequencies and V_{DC}.

Finally, as mentioned earlier, this phenomenon at high frequencies and V_{DC} could be related to the experimental setup. It is suggested that at low impedance and high frequencies, the connected components such as the opamps and cables affect the measurement and lead to instability.

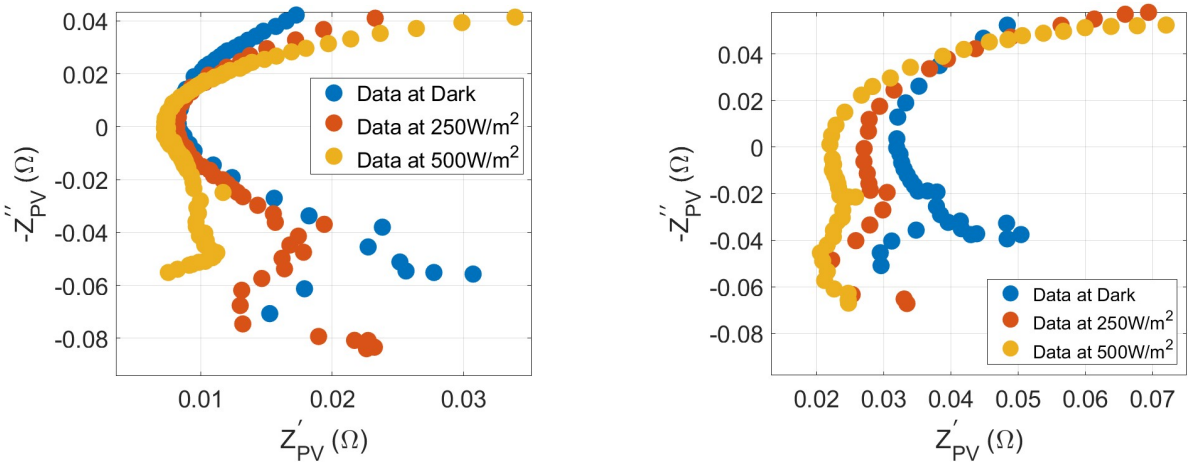

(a) IBC **(b)** PERC

Figure 4.10: Nyquist spectra of IBC and PERC cells at V_{DC} = 619.5 and 539mV, respectively, T = 30°C and in dark, 250 and 500W/m^2 (zoomed-in).

4.2. Capacitance results

This section will introduce and explain the capacitive impedance of IBC and PERC cells. Various plots will be presented to depict the effects of temperature, illumination, and applied voltage on the junction capacitance. Finally, the effect of temperature and illumination on the maximum power point (MPP) and junction impedance at this point will be studied and discussed.

4.2.1. Temperature-dependent variation of C_j

In Figure 4.11, the junction capacitance (C_j) is plotted as a function of temperature for IBC and PERC cell laminates. The plots were made at 0, 539 and 619.5mV since 539 and 619.5mV are the MPP's for PERC and IBC cells under STC, respectively. Furthermore, the temperature range was chosen to be between 25 and 60°C with 5°C intervals. Additionally, the experiment was performed in absence of light and under 500W/m^2. From Figure 4.11a and 4.11c, it is noted that C_j increases as the temperature is increased. However, the rate of increment depends on the condition in which the cell is operating. For example, at 0W/m^2 and 0mV the impact of temperature on C_j is negligible compared to data at 619.5mV as shown in Figure 4.11a. Moreover, by comparing the data at 0W/m^2 and 0mV (blue line) with 500W/m^2 and 0mV (red line), it is also noted that the impact is insignificant. On the other hand, at 0W/m^2 and 619.5mV (green line) and at 500W/m^2 and 619.5mV (black line) the impact is higher. Thus, the effect of temperature on C_j increases at higher applied voltages. To understand this behavior, it is important to remember that at low V_{DC}, C_j is dominated by C_{dep} while at high V_{DC} by C_{diff}. As explained earlier, n_i increases with increasing temperatures according to equation 4.1. This increase will influence V_{bi} according to the following equation [3]:

$$V_{bi} = \frac{k_B T}{q} \ln\left(\frac{N_a N_d}{{n_i}^2}\right) \tag{4.3}$$

So, n_i increases with temperature increase which decreases V_{bi}. Consequently, C_{dep} (see eq. 2.14) will increase due to the decrease of V_{bi} while the other parameters are kept constant.
At high V_{DC}, $C_j \approx C_{diff}$. According to eq. 2.15, C_{diff} is directly dependent on n_i and therefore it will increase as the temperature increases. It is worth noting that C_{diff} has a stronger dependency on n_i compared to C_{dep}, therefore C_j increases at a higher rate with temperature increase as shown in Figure 4.11a. Furthermore, it is important to mention that the data points at 55 and 60°C of the black line shown in Figure 4.11a were fitted for f $\leq$ 10kHz because the equivalent model was not able to find suitable fitting-values for higher frequencies data. Similarly, this also holds for the data points at 50, 55 and 60°C of the green line.

Finally, the same explanation holds for PERC cell plots demonstrated in Figure 4.11b. It is important to note that at 539mV, 0W/m^2 and 60°C, the model was not able to find suitable fitting-values. In addition, an attempt was made to fit the data with lower frequencies but the obtained value was relatively low. Therefore, it was decided to ignore this value.

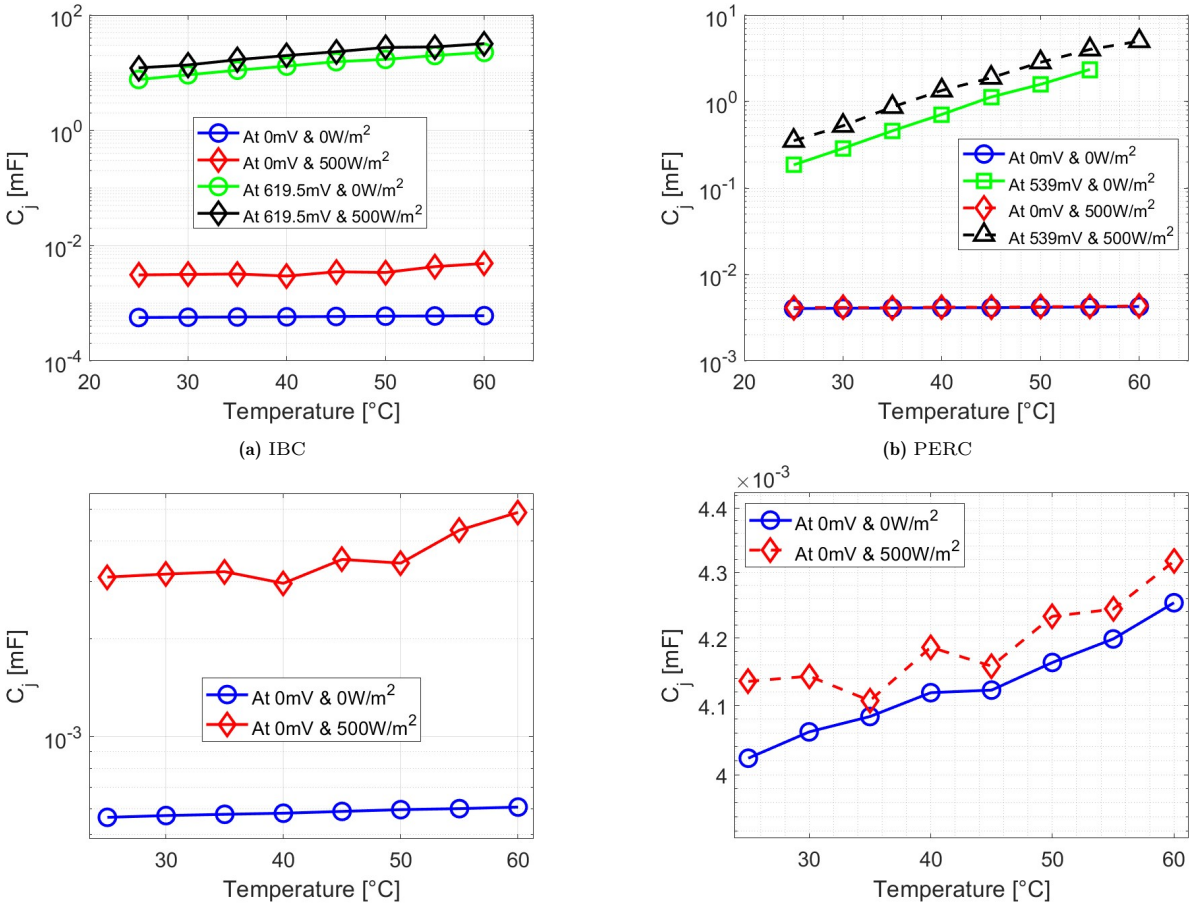

(a) IBC

(b) PERC

(c) IBC (zoomed-in)

(d) PERC (zoomed-in)

Figure 4.11: C_j as a function of temperature for IBC and PERC cells at different V_{DC} and illumination levels.

4.2.2. Illumination-dependent variation of C_j

In order to study the impact of illumination on C_j, the intensity versus C_j is plotted as illustrated in Figure 4.12. The plots are taken at intensities from 0 to 500W/m^2 with 100W/m^2 intervals for IBC cell while it goes from 0 to 700W/m^2 with 100W/m^2 intervals for PERC cell. Since PERC cell generates less current compared to IBC cell, it was possible to reach 700W/m^2 without the need to shorten the distance between the LED and the cell which results in a non-uniform illumintaion. Furthermore, the plots are taken at the same voltages as for the temperature sweep experiment and at 30 and 60°C. Similarly, $C_j \approx C_{dep}$ at 0mV while for 619.5 and 539mV, $C_j \approx C_{diff}$. In general, the illumination does not affect C_j directly according to eqs. 2.14 and 2.15. However, at higher light intensity, additional electron-hole pairs are generated at each side of the PN junction. This results in a higher charge in the depletion region. Consequently, the width of the depletion region will decrease leading to a higher C_j value [28]. This relation could also be explained by Mott-Schottky expression [14]:

$$C_j \approx \sqrt{\frac{\epsilon |q| N}{2(V_{bi} - V_j)}} \tag{4.4}$$

where N is the doping concentration and equals N_d or N_a depending on the cell type, V_j is the voltage drop over the PN junction. By increasing the illumination level, V_j will increase resulting in a higher C_j. It is important to note that this equation only holds at low bias voltages where $C_j \approx C_{dep}$. Furthermore, by comparing Figure 4.12a and 4.12b it is observed that illumination affects IBC cell more than PERC cell at 0mV. This is due to the differences in doping concentrations of the selective emitter and bulk of both cells and differences in the generated V_j by the illumination.

At high forward bias, $C_j \approx C_{diff}$ and the relation between the C_j and the intensity can be described as follows [14]:

$$C_j = \beta \exp\left(\frac{|q|V_j}{nk_BT}\right) \tag{4.5}$$

where β is a constant independent of illumination. Similarly, V_j will increase by increasing intensity leading to an increase in C_j at high forward bias.

Finally, this explanation holds for both cells taking into account the difference in the applied voltage. Furthermore, the data points at 593 and 619.5mV were executed only for f $\leq$ 10kHz in order to obtain reasonable fitting-values.

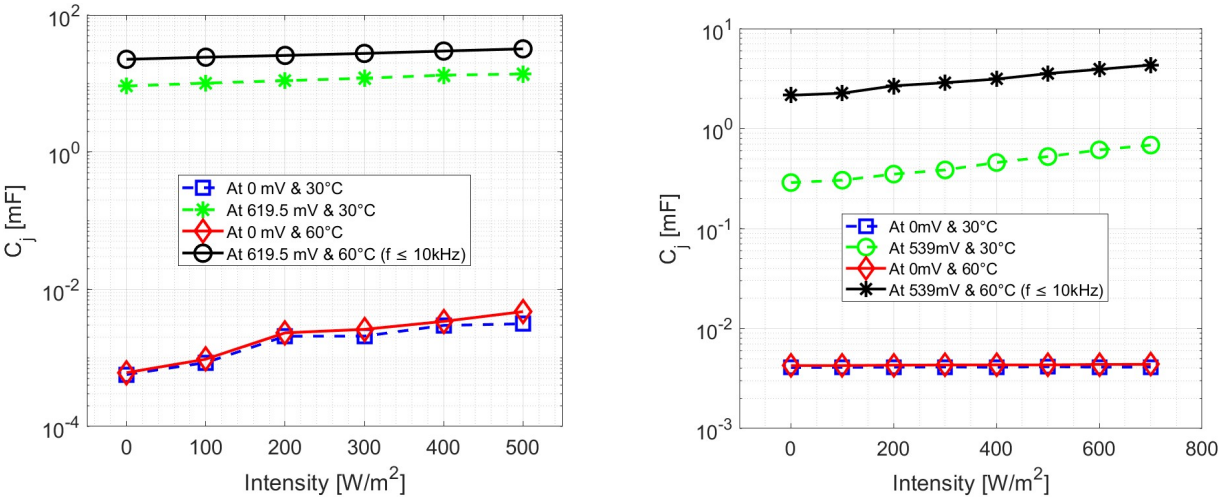

(a) IBC **(b)** PERC

Figure 4.12: C_j as a function of intensity for IBC and PERC cells at different V_{DC} and temperatures.

4.2.3. Voltage-dependent variation of C_j

The relation between C_j and V_{DC} is another aspect to investigate in this thesis project. Figure 4.13 shows the C_j-V_{DC} plots in absence of light and at T = 30, 45 and 60°C for IBC and PERC cells. For both cells, it is observed that C_j in high forward bias increases exponentially with increasing V_{DC} due to the exponential dependency of C_{diff} on V_{DC} (see eq. 2.15). In Figure 4.13, it is again observed that C_j increases with a higher rate at high forward bias compared to low forward bias. The impact of temperature is higher at high V_{DC} ranges since the temperature affects C_{diff} stronger than C_{dep} as explained before. In Figure 4.13a, it is worth noting that the data points at 619.5, 625 and 650mV (at 60°C) and at 625 and 650mV (at 45°C) are fitted until f $\leq$ 10kHz in order to obtain reasonable fitting-values. Similarly, the data point for PERC cell at 539mV (at 60°C) was also fitted until f $\leq$ 10kHz. This indicates that at 539mV the equivalent model was unable to fit the data while 550mV was fitted properly. This suggests that the data could be influenced by the experimental setup.

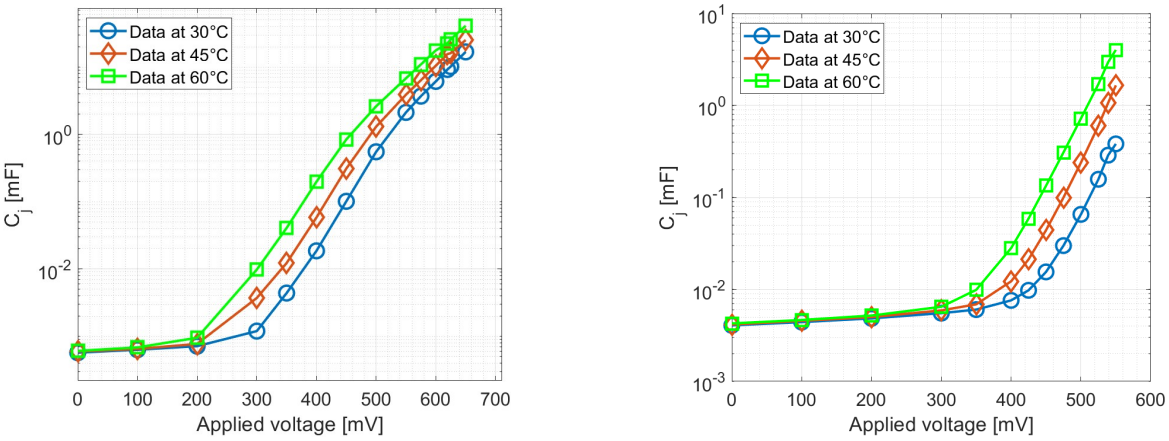

(a) IBC **(b)** PERC

Figure 4.13: C_j as a function of V_{DC} for IBC and PERC cells in absence of light and at different temperatures.

Another important part to investigate is the impact of illumination on the C_j-V_{DC} relation. In Figure 4.14, C_j-V_{DC} plots are shown for different illumination levels. Starting with the high V_{DC} region, it is noted that the illumination slightly affects C_{diff} for both cells. For PERC cell, illumination shows even a smaller impact at the low V_{DC} region as shown in Figure 4.14b. On the other hand, for IBC cell, the illumination affects C_{dep} (at low V_{DC}) more than C_{diff} (at high V_{DC}) as depicted in Figure 4.14a. This could be related to the differences in the structure and doping concentrations of IBC compared to PERC cell. Furthermore, it could be due to the fitting model which becomes less accurate for IBC cell at higher illumination levels and low forward bias voltages as shown in Figure 4.7.

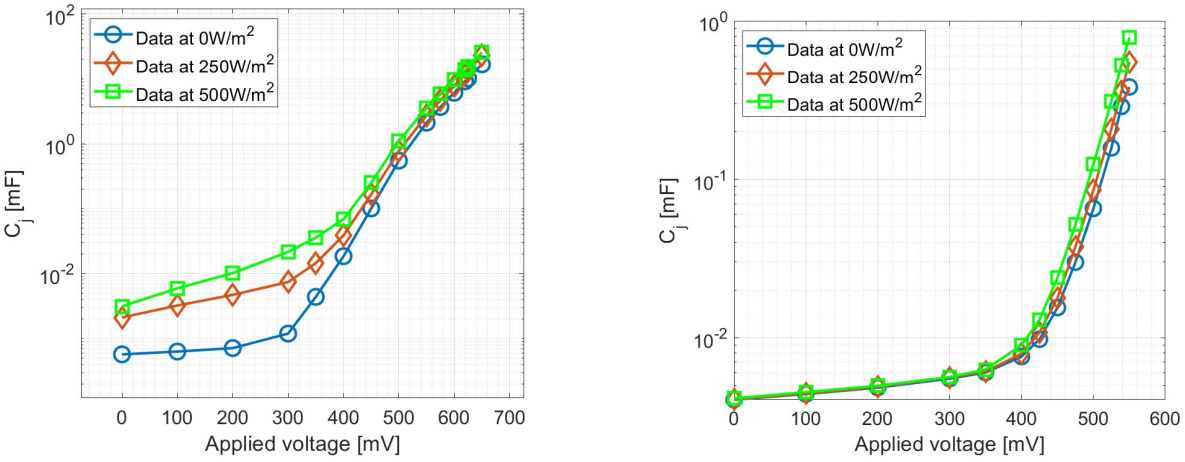

(a) IBC **(b)** PERC

Figure 4.14: C_j as a function of V_{DC} for IBC and PERC cells at 30°C and different illumination levels.

4.2.4. MPP experiment

When the illumination level, temperature or both are changed, the MPP of the PV cell will change accordingly. This is observed on Figures B.5 and B.6 in Appendix B.4, where the power is shown as a function of voltage. More specifically, V_{MPP} decreases with increasing temperature, while it increases with increasing illumination level as depicted in Figure 4.15. When the temperature rises, n_i and J_0 increase accordingly, leading to a lower V_{oc} as discussed earlier. Similarly, V_{oc} decreases with decreasing illumination levels as $V_{oc} = V_j + V_{LH}$, where V_{LH} is the voltage drop across the LH junction [14]. This decrease in V_{oc} leads to a decrease in V_{MPP}. As a result, C_j will also change due to its dependency on the applied voltage. Therefore, it is essential to study the behavior of C_j at the MPP of different conditions. Figure 4.16 shows two plots presenting the temperature on horizontal axis, illumination on vertical axis and C_j represented as a color. From both plots, it can be concluded that increasing the intensity (while maintaining a consistent temperature), leads to a significant increase in C_j. This can be explained using Figure 4.15 which shows how $V_{DC,MPP}$ increases with increasing illumination. Since C_{diff} is exponentially dependent on V_{DC}, C_j increases significantly (according to eq. 2.15). Additionally, increasing the temperature (while keeping the intensity constant) also increases C_j due to the increment in n_i as mentioned earlier. However, this increment in C_j is low compared to the increment caused by the illumination since increasing the temperature leads to a lower $V_{DC,MPP}$ as shown in Figure 4.15. Moreover, it is observed that increasing the temperature and n_i has more impact on C_j than the reduced $V_{DC,MPP}$ due to the same temperature increment.

Finally, this experiment revealed that, on average, C_j increases by approximately 1.03 times for every 10°C rise in temperature and by roughly 1.29 times for every 100W/m^2 increase in irradiance for IBC cell. Furthermore, for PERC cell, C_j increases by approximately 1.1 and 1.57 times for every 10°C and 100W/m^2 increment, respectively. In this experiment, the minimum C_j values are 45μF and 3.1mF for PERC and IBC, respectively. According to [11], the minimum required input capacitance of a DC-DC boost converter can be calculated as follows:

$$C_{in} = \frac{I_{mpp}\gamma_{I_L}}{8V_{mpp}\gamma_{V_{mpp}}f} \tag{4.6}$$

where I_{mpp} is the current at MPP, γ_{I_L} the inductor current ripple factor, V_{mpp} the voltage at MPP, $\gamma_{V_{mpp}}$ voltage ripple at MPP and f the switching frequency. To calculate C_{in} for IBC and PERC cells, the values of Impp and Vmpp in Table 3.2 has been used. Furthermore, by setting f at 100kHz, γ_{I_L} at 10% and $\gamma_{V_{mpp}}$ at 1% (typical values) [11], the following results were obtained: $C_{in,IBC} \approx 104\mu$F and $C_{in,PERC} \approx 81\mu$F. Since $C_{in,IBC} < 3.1$mF and $C_{in,PERC} > 45\mu$F (see Figure 4.16a and 4.16b), it can be concluded that a single IBC cell has a higher potential than a single PERC cell to be used as an input capacitor. However, the capacitance of a PERC cell string could be high enough to serve as an input capacitor even at low illumination levels and temperatures.

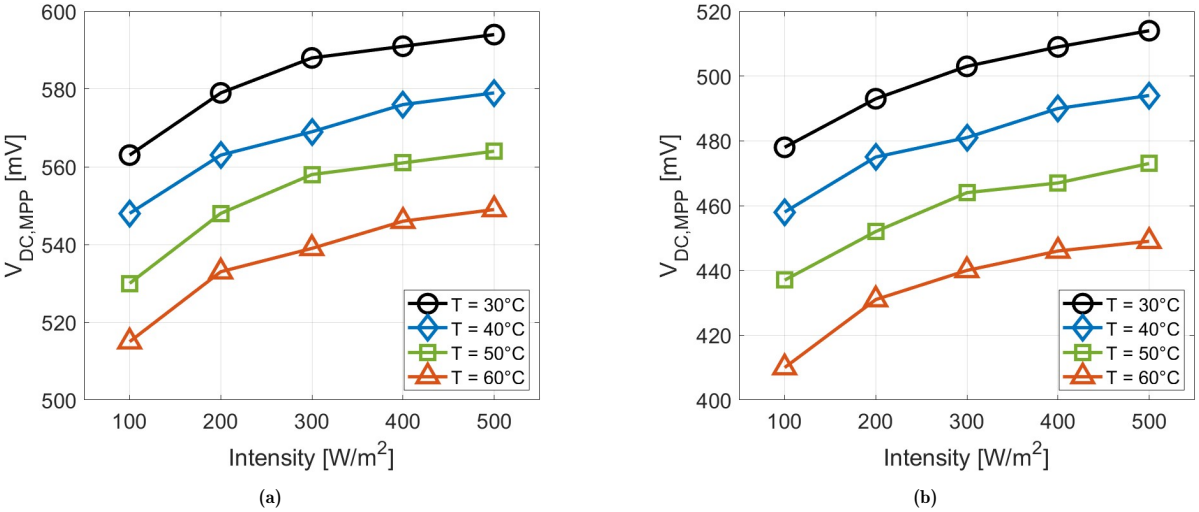

Figure 4.15: $V_{DC,MPP}$ as a function of intensity at different temperatures for (a) IBC and (b) PERC.

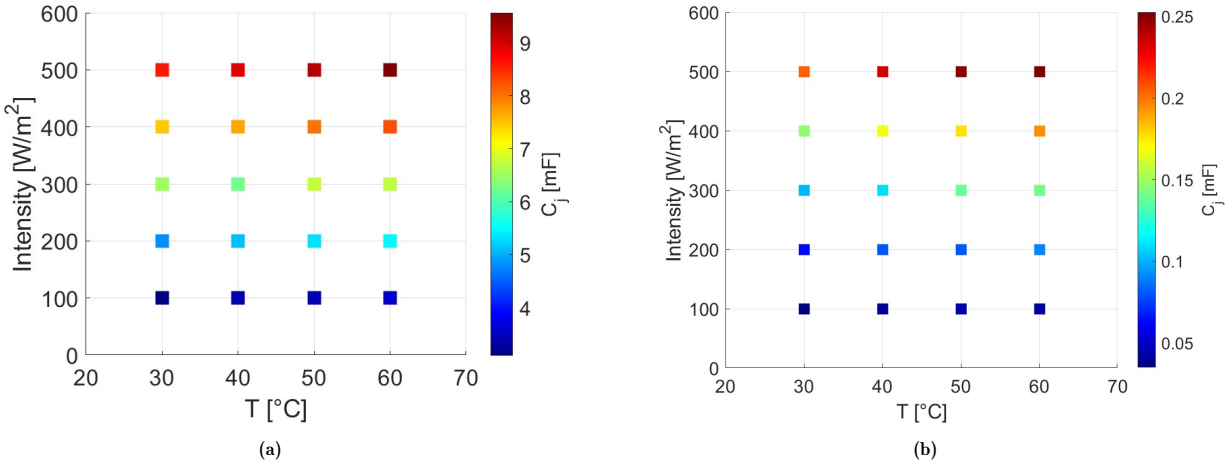

Figure 4.16: A heatmap of C_j at different temperatures and illumination levels for (a) IBC and (b) PERC cells.

4.3. CPE Nyquist spectra

In section 2.5, the CPE component was introduced and explained. The first intention was to include and apply this component in the equivalent circuit in order to improve the fitted data. In the following section, some results of the new proposed model will be presented and discussed.

In order to study the effect of CPE component on the fitting, specific impedance data were selected namely, for IBC cell at 600mV, 30°C and under an illumination of 500W/m^2. The IBC cell was selected as its fitting showed more deviations than the fitting of PERC under higher illumination. At the beginning, all the equivalent model components shown in Figure 2.14 were considered as fitting parameters. The initial value of n was set at 0.5. Furthermore, the lower and upper bounds of n were equal to 0 and 1, respectively. However, the model was not able to fit the data properly. Therefore, another approach was used to perform the fitting. So, all the fitting parameters were fixed except n. Then, the data was fitted with different n values ranging from 0 to 1 with 0.2 intervals as shown in Figure 4.17a. It was noted that for $0.5 < n < 0.6$, the fitting could be optimized as shown in Figure 4.17b. Therefore, the lower and upper bounds were adjusted to 0.5 and 0.6, respectively. Furthermore, the initial value of n was set at 0.55. This trial and error process was repeated many times where the upper bound was fixed to 0.6, while the initial value of n and the lower bound were changed every time. At the end, the n parameter was fitted by the CNLS algorithm at $n = 0.592$ as illustrated in Figure 4.18. To evaluate the fitting of the new model, the error values of the old and new model were compared to each other. As a result, it was noted that $RMSE_\theta$ and $NRMSE_R$ reduced from 3.234 and 0.0103 to 1.931 and 0.0060, respectively. This significant reduction can be seen in Figure 4.19 which compares the fitting of the original model and the CPE model. It is also noted that the CPE component provides more freedom to the model to fit the variations in the high frequency range of the impedance spectrum.

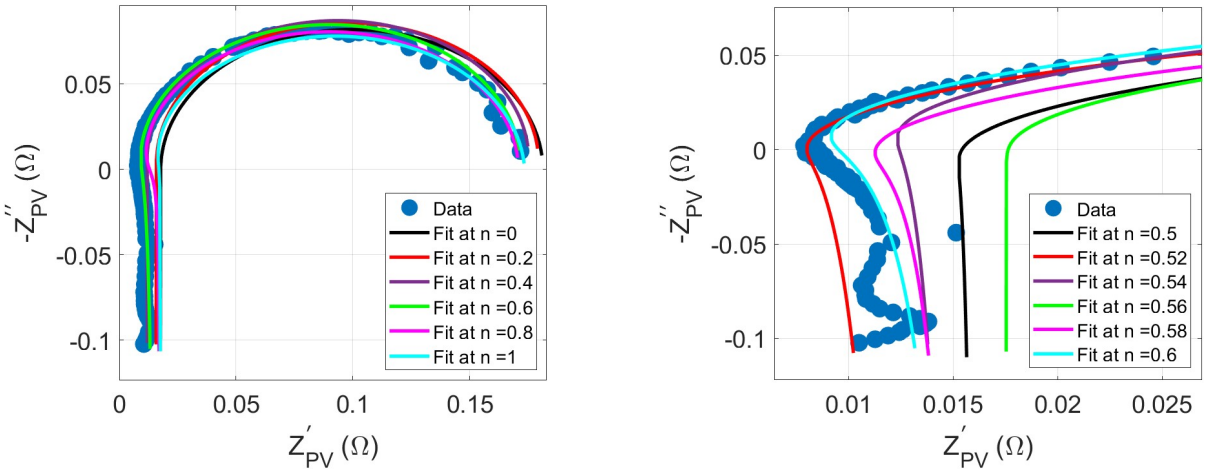

Figure 4.17: Impedance data for IBC cell at 600mV, 500W/m^2 and 30°C with, (a) n = 0 to 1 and (b) n = 0.5 to 0.6.

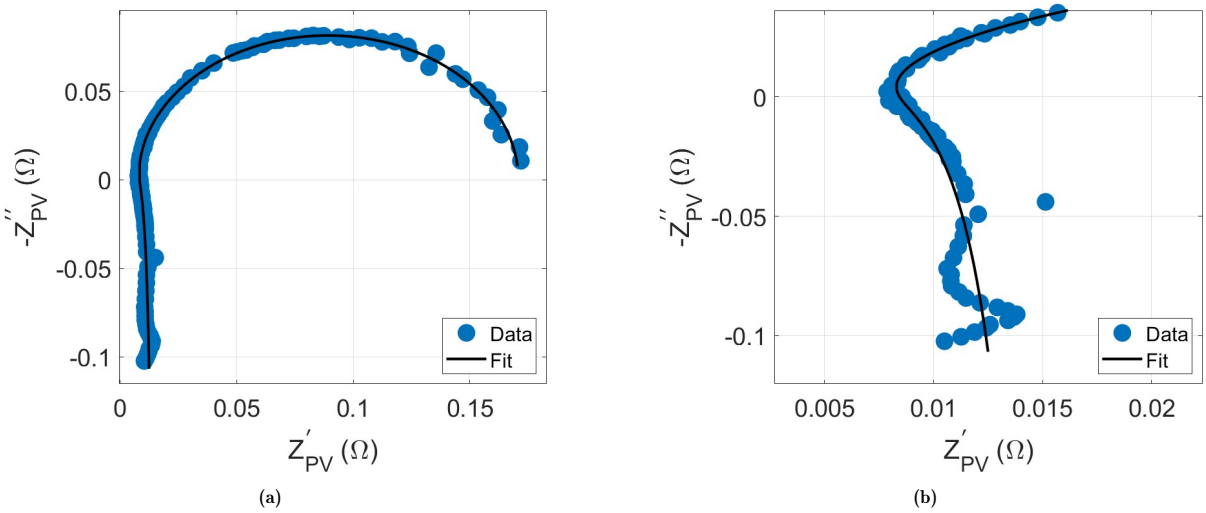

Figure 4.18: Impedance data for IBC cell at 600mV 500W/m^2 and 30°C with, (a) n = 0.592 and (b) n = 0.592 (zoomed-in).

Although the CPE model shows promising results, more research has to be done in order to improve it. One of the challenges in the current CPE model is the fitting-values, especially the value of the CPE component. The model is unable to find accurate fitting-values automatically since there are many fitting parameters which increases the complexity of the model. It was mentioned earlier that all the fitting parameters were fixed except n. These values were taken from an initial fitting trial and error process. The obtained CPE value was 524.8kF which has no physical meaning. From a further investigation, it was noted that the CPE value could decrease by changing the boundary conditions and initial values of the other parameters or by decreasing the upper bounds of the CPE component. Additionally, an attempt was made to find a global value for n and consequently use it as an initial value. However, this effort did not achieve success. It is also important to note that there could have been instances of undiscovered implementation errors in the model which could lead to such high CPE values.

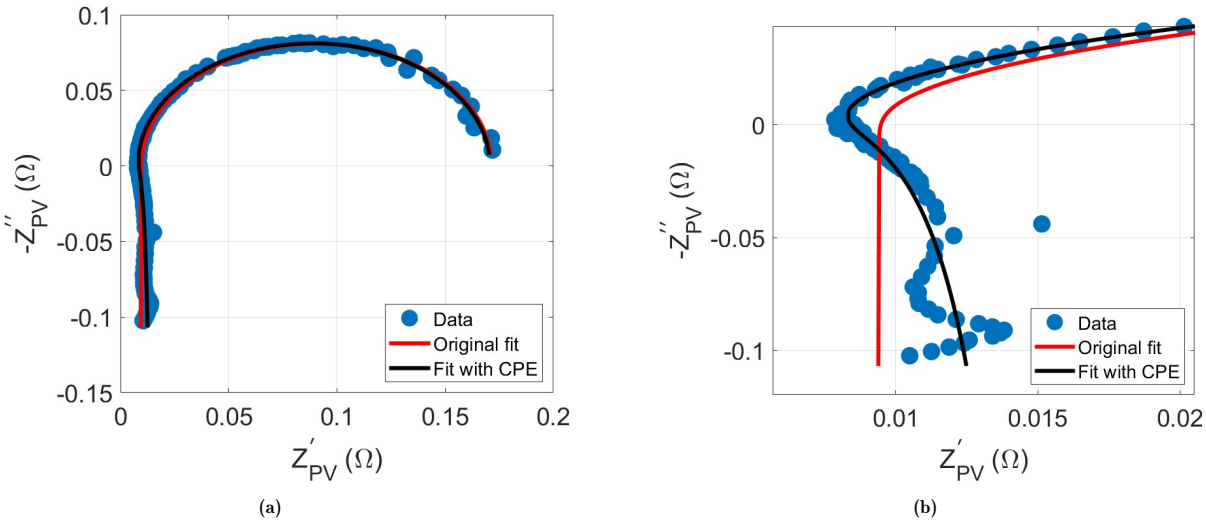

Figure 4.19: Impedance data for IBC cell at 600mV, 500W/m^2 and 30°C illustrating the difference between the fitting of the original model and the CPE model with, (a) complete figure and (b) zoomed-in.

Finally, an attempt was made to improve the model by replacing the second R-C loop with another R-Z_{CPE} loop. In other words, the model will consist of two R-Z_{CPE} loops, R_s and L_s connected in series. Furthermore, two approaches were used to fit the data. The first approach was by assuming that the n parameter is the same for both CPE components, while the second approach assumed that

each CPE component has its own n value. Also, there were more attempts to change the value of n manually in order to optimize the fitting. However, these attempts did not achieve success and resulted in high error values. Again, there could have been instances of undiscovered implementation errors in the model which could lead to such high error values. In conclusion, a fitting model with one CPE component shows more promising results compared to two CPE components model. Furthermore, this model requires more research in order to optimize the new fitting model.

5

Conclusion and recommendations

In this thesis, the influence of temperature and illumination on the impedance of the IBC and PERC cell laminates has been examined and analyzed. In this chapter, the main findings of this thesis project will be summarized, aligning them with the research objectives outlined in Section 1.6. The main conclusions derived from this study will be addressed in Section 5.1, followed by recommendations regarding future research on optimization and improvement possibilities in Section 5.2.

5.1. Conclusions

The first objective of this research was to determine an appropriate impedance model that can describe the dynamic electrical behavior of c-Si PV cells under real-world operating conditions. As a starting point, a commonly used model which consists of two R-C loops, R_s and L_s has been utilized. The model was used to fit impedance data at different temperatures and illumination levels. Firstly, the impedance data at 30°C, in absence of light and various V_{DC} have been chosen as a reference to examine the used model. Under these conditions, the model seems to perform well which can be verified by the low error values. However, at a specific range, where R_{LH}-C_{LH} loop impedance is relatively high compared to R_j-C_j loop impedance, the fitting model was less accurate. This was also verified by the calculated error values. This problem is mainly observed for IBC cell which is presumably related to differences in the design and doping concentrations of this cell compared to PERC cell. Secondly, the fitting model was examined in absence of light, different V_{DC} and at different temperatures, namely T = 30, 45 and 60°C to study the impact of the temperature on the Nyquist spectra. As a result, it was concluded that the impedance decreases with increasing temperatures. This was also verified by analyzing the slope of the I-V curves. In addition, it was observed that the fitting model becomes less accurate at high V_{DC} and higher temperatures. For instance, at T = 60°C and V_{DC} = 619.5mV (MPP of IBC), the model was not able to fit the data. This observation is valid for both cell laminates. Thirdly, the fitting model was also tested at different illumination levels to understand how illumination affects the Nyquist spectra. This was done at T = 30°C, different V_{DC} values and intensity = 0, 250 and 500W/m^2. Similarly to temperature experiment, it was observed that the impedance decreases with increasing illumination levels. Moreover, it was noted that the fitting model becomes less accurate at V_{DC} = 200mV and higher intensities, since the R_{LH}-C_{LH} loop impedance becomes more prominent compared to R_j-C_j impedance even at low bias voltages. This phenomenon is associated with R_{sh} which decreases at higher illumination levels. Fourthly, it was noted that the impedance data exhibit an unusual trend at high V_{DC} and high frequencies. This trend affects the fitting process significantly, resulting in less accurate results. The main reason of this phenomenon is still uncertain but it might be related to the influence of the experimental setup on the measured data. Up until now, it can be concluded that the used fitting model operates with sufficient accuracy at only specific conditions. Furthermore, in order to fit the impedance data at higher temperatures and illuminations levels, the current model has to be modified. Therefore, a new model was proposed which uses a CPE component instead of a capacitor. The CPE component is capable of explaining the deviations from ideal behavior in cell capacitances resulting from disordered junctions or systems with traps at different energy levels and spatial regions. The new model consists of R-C loop, R-Z_{CPE} loop, R_s and L_s. This model was tested on IBC cell at 600mV, 30°C and 500W/m^2.

As a result, the error values were reduced significantly compared to the other fitting model. However, the fitting values obtained by this model had no physical meaning, especially the value of CPE itself. In conclusion, although the model with CPE component shows promising results, it still requires further research to optimize it such that it can find reasonable values for the fitting parameters automatically.

The second objective of this thesis was to asses the impact of temperature on the impedance of a single solar cell. To study this, experiments were executed at T = 25 to 60°C with intervals of 5°C, in absence of light and at an illumination of 500W/m^2. Furthermore, two V_{DC} values were chosen for each cell, namely 0 and 539mV, and 0 and 619.5mV for PERC and IBC cells, respectively. Then, the PN junction capacitance (C_j) was plotted as a function of temperature. In conclusion, for IBC cell at high forward bias and in dark conditions, C_j increased from 7.6mF at 25°C to 22.6mF at 60°C, while it increased from 0.56μF at 25°C to 0.61μF at 60°C at low forward bias. Similarly, for PERC cell, at high forward bias and in dark conditions, C_j increased from 0.19mF at 25°C to 2.4mF at 55°C (data at 60°C was not reliable), while at low forward bias, it increased from 4μF at 25°C to 4.3μF at 60°C. These differences in the increment rates at low and high forward biases are caused by the strong dependency of C_{diff} ($\approx C_j$ at high V_{DC}) on temperature, while the effect of temperature on C_{dep} ($\approx C_j$ at low V_{DC}) is negligible. Finally, C_j was plotted as a function of V_{DC} at T = 30, 45 and 60°C and in absence of light. From these plots, it was proven that the impact of temperature on C_j is higher at high forward bias voltages, while it is negligible at low forward bias.

The third objective of this thesis was to investigate how the impedance of a single solar cell changes under varying illumination levels. For this experiment, C_j was plotted as a function of intensity which was chosen to span from 0 to 500W/m^2 for IBC cell, while it spans from 0 to 700W/m^2 for PERC cell. Additionally, the experiments were executed at T = 30 and 60°C. Moreover, V_{DC} was chosen to be 0, 539 (for PERC) and 619.5mV (for IBC). From this experiment, it was observed that for IBC cell at high forward bias and 30°C, C_j increased from 9.2mF in dark conditions to 13.8mF at 500W/m^2. Furthermore, for IBC cell and low forward bias, C_j increased from 0.6μF in dark conditions to 3.1μF at 500W/m^2. Similarly, for PERC cell at high forward bias and 30°C, C_j increased from 0.3mF in dark conditions to 0.7mF at 700W/m^2, while it increased from 4.06μF to 4.11μF at low forward bias. In addition, it was noted that at low forward bias, the increment is higher for IBC cell than PERC. Again, this difference is mainly associated with the structure and doping concentration differences in bulk and selective emitter layers between the two cells. Similarly to the second objective, C_j was plotted as a function of V_{DC} at 0, 250 and 500W/m^2 and T = 30 °C. In conclusion, the impact of the illumination on C_j was higher at high forward bias than low forward bias for PERC cell. In contrast, the impact of illumination on C_j was stronger at low forward bias than high forward bias. This is mainly related to the cell design and the doping concentrations of the bulk and selective emitter of each cell. Furthermore, it could also be related to the fitting model which becomes less accurate for IBC at higher illumination levels and low forward bias.

The fourth objective of this thesis was to examine the impact of temperature and illumination on the impedance of a PV cell at its maximum power point. To do this, I-V curves were measured to determine the $V_{DC,MPP}$ values for T = 30 to 60°C with intervals of 10°C and for an intensity range spanning from 100 to 500W/m^2 with intervals of 100W/m^2. Then, C_j at maximum power point voltage was plotted as a function of temperature and intensity for both cells. From the plots, it is observed that C_j operates between 3 and 9.5mF for IBC cell, while the range is lower for PERC cell and spans from 0.045 to 0.25 mF. In addition, it was concluded that increasing the intensity (while keeping the temperature constant), increases C_j more significantly compared to the increase in temperature. Furthermore, C_j increases approximately by a factor of 1.03 for every 10°C rise in temperature and by roughly 1.29 times for every 100W/m^2 increase in irradiance for IBC cell. Moreover, for PERC cell, C_j increases by approximately 1.1 and 1.57 times for every 10°C and 100W/m^2 increment, respectively. Finally, the main goal of this thesis project was to investigate the impact of temperature and illumination on the C_j to determine whether it can replace the input capacitor of a DC-DC converter. As a result, it was proven that the C_j of a single IBC cell laminate has a higher potential than a single PERC cell to serve as an input capacitor. However, the capacitance of a PERC cell string could be high enough to fulfil this function even at low illumination levels and temperatures. Furthermore, a single PERC cell might still be useful for other applications such as visible light communication.

5.2. Recommendations

This section outlines recommendations for future researches. These avenues were not explored during this thesis project due to time constraints.

Firstly, it is important to verify whether the experimental setup has an impact on the impedance data at high frequencies and voltages. This recommendation is a priority as it could improve the fitting data significantly. Furthermore, it might obviate the necessity for a new fitting model.

Secondly, it is essential to further investigate the fitting model in order to obtain accurate fitting values under different temperatures and illumination levels. Additionally, it is strongly recommended to start with the proposed CPE model. This model showed a significant potential for improvements due to its increased flexibility and relaxed nature compared to the currently used model. Furthermore, it would be valuable to use two CPE components instead of one. However, this might be more complex as more attention for the initial values and boundary conditions has to be considered.

Finally, it would be interesting to study the behavior of a fitting model that consists of one R-Z_{CPE} loop and two R-C loops. According to [18], such a model is able to fit the impedance data under different illumination levels properly.

A

Appendix A

According to the final model shown in figure 2.12, the total impedance of the solar cell can be expressed as follows:

$$Z_{PV} = R_s + j\omega L_s + \left[R_j || \frac{1}{j\omega C_j}\right] + \left[R_{LH} || \frac{1}{j\omega C_{LH}}\right] \tag{A.1}$$

working out equation A.1 gives:

$$\begin{aligned}\left[R_j || \frac{1}{j\omega C_j}\right] &= \frac{\frac{R_j}{j\omega C_j}}{R_j + \frac{1}{j\omega C_j}} \\ &= \frac{\frac{R_j}{j\omega C_j}}{\frac{1+j\omega R_j C_j}{j\omega C_j}} \\ &= \frac{R_j}{1 + j\omega R_j C_j}\end{aligned}$$

then we multiply this by $\frac{1-j\omega R_j C_j}{1-j\omega R_j C_j}$ which gives:

$$\left[R_j || \frac{1}{j\omega C_j}\right] = \frac{R_j - j\omega R_j^2 C_j}{1 + \omega^2 R_j^2 C_j^2}$$

similarly,

$$\left[R_{LH} || \frac{1}{j\omega C_{LH}}\right] = \frac{R_{LH} - j\omega R_{LH}^2 C_{LH}}{1 + \omega^2 R_{LH}^2 C_{LH}^2}$$

Finally, equation A.1 can be rewritten into the form $Z_{PV} = Z'_{PV} + jZ''_{PV}$ where Z'_{PV} is the resistance and Z''_{PV} is the reactance:

$$Z'_{PV} = R_s + \frac{R_j}{1 + \omega^2 R_j^2 C_j^2} + \frac{R_{LH}}{1 + \omega^2 R_{LH}^2 C_{LH}^2} \tag{A.2}$$

$$Z''_{PV} = \omega L_s - \frac{\omega R_j^2 C_j}{1 + \omega^2 R_j^2 C_j^2} - \frac{\omega R_{LH}^2 C_{LH}}{1 + \omega^2 R_{LH}^2 C_{LH}^2} \tag{A.3}$$

B

Appendix B

B.1. Nyquist plots and best-fit values for PERC cell

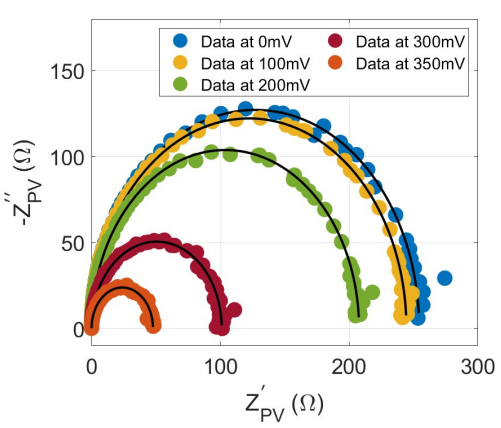

(a) Applied V_{DC} from 0 to 350mV

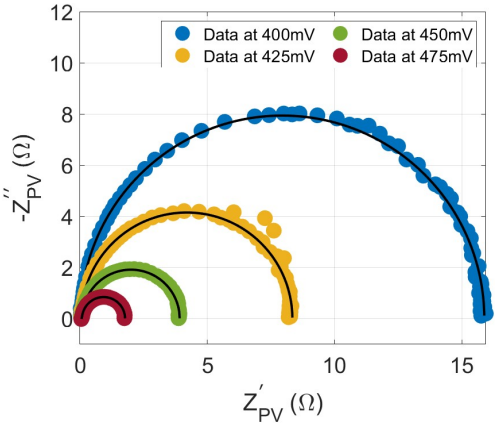

(b) Applied V_{DC} from 400 to 475mV

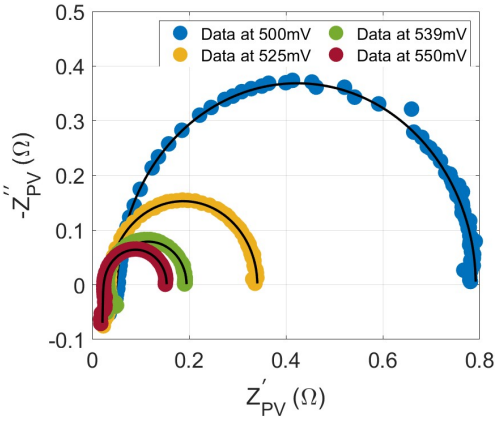

(c) Applied V_{DC} from 500 to 550mV

Figure B.1: Nyquist spectra for the PERC cell laminate with V_{DC} gradually increasing from 0 to 550mV at 30°C and in dark.

Table B.1: Best-fit values for the PERC cell laminate in dark and at 30°C.

V_{DC} (mV)	C_j (μF)	R_j (Ω)	C_{LH} (μF)	R_{LH} (mΩ)	R_s (mΩ)	L (nH)	$NRMSE_M$ (-)	$RMSE_\theta$ (-)	$NRMSE_R$ (-)	$NRMSE_X$ (-)
0	4.061	244.5	-	-	-	-	0.0044	0.6686	0.0052	0.0130
100	4.406	254.3	-	-	-	-	0.0097	0.8827	0.0094	0.0212
200	4.836	207.7	-	-	-	-	0.0066	0.8662	0.0073	0.0198
300	5.515	101.1	-	-	-	-	0.0135	1.1001	0.0137	0.0257
350	6.030	47.73	-	-	-	-	0.0099	1.2851	0.0095	0.0183
400	7.599	15.88	0.0081	5.022	3.490	72.75	0.0054	2.3576	0.0051	0.0103
425	9.778	8.299	0.0003	37.03	6.755	41.51	0.0161	1.4434	0.0136	0.0244
450	15.49	3.831	12.997	81.23	3.435	95.23	0.0074	0.9721	0.0070	0.0093
475	29.93	1.692	12.605	74.38	3.467	117.1	0.0053	0.9741	0.0052	0.0079
500	65.45	0.741	13.783	46.81	4.090	120.3	0.0092	1.0379	0.0092	0.0085
525	157.6	0.310	16.184	22.24	8.542	118.6	0.0072	1.4170	0.0068	0.0068
539	288.2	0.161	0.3626	20.47	13.45	79.74	0.0294	5.5924	0.0280	0.0367
550	382.4	0.132	24.140	12.82	9.144	100.8	0.0123	1.9977	0.0124	0.0104

B.2. Effect of temperature on the impedance of PERC cell

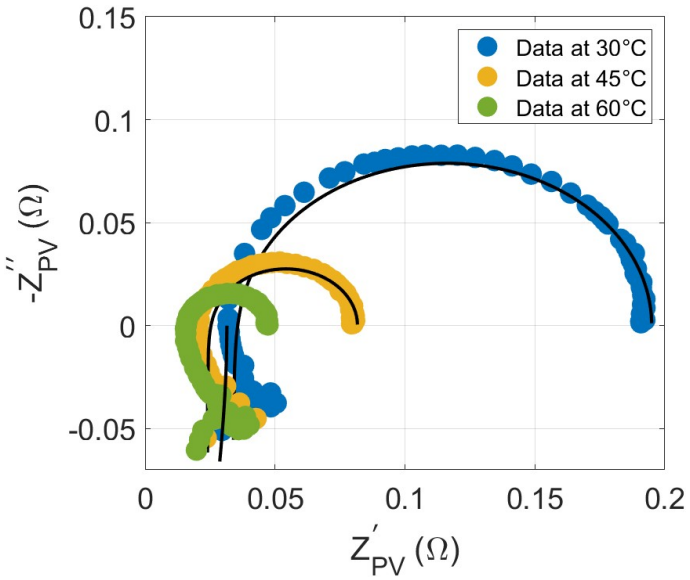

Figure B.2: Nyquist spectra of PERC cell in dark, at 539mV and different temperatures.

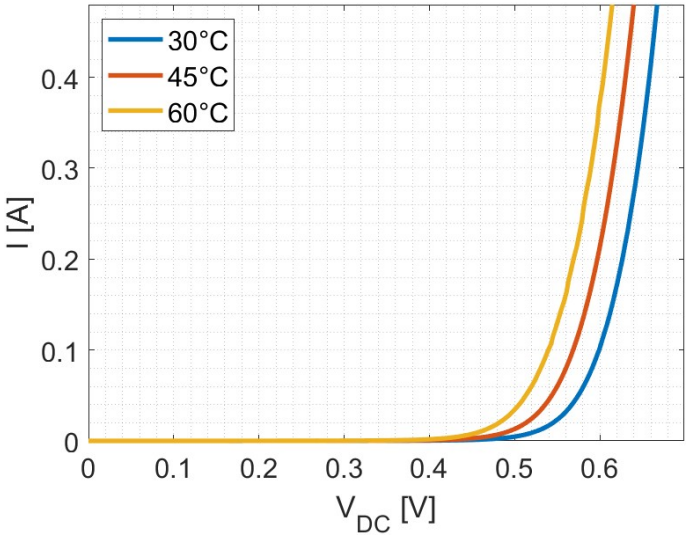

Figure B.3: I-V curves of PERC cell in dark at V_{DC} = 539mV and T = 30, 45, 60°C.

B.3. Effect of illumination on the impedance of PERC cell

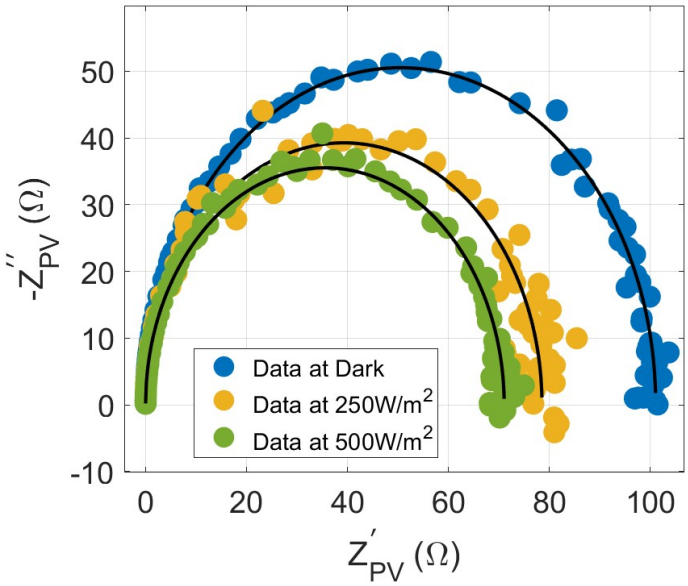

Figure B.4: Nyquist spectra of PERC cell at V_{DC} = 300mV, T = 30°C and intensity = 0, 250 and 500W/m^2.

B.4. Effect of illumination and temperature on the MPP of PV cell

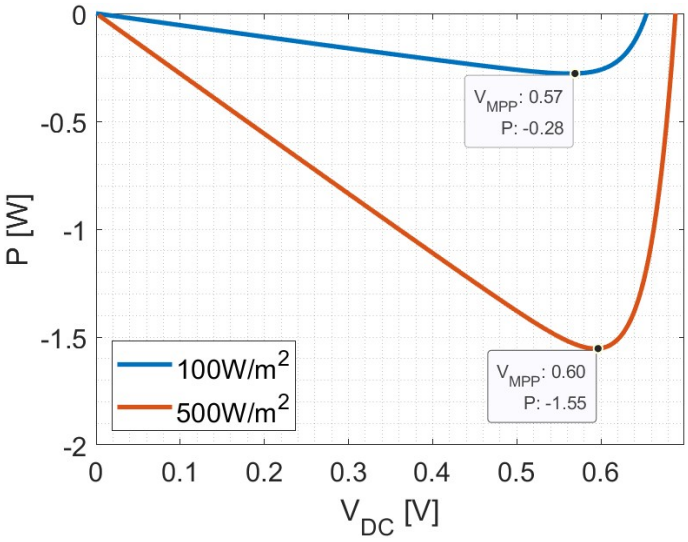

Figure B.5: Effect of the illumination level on the power of IBC cell at 30°C.

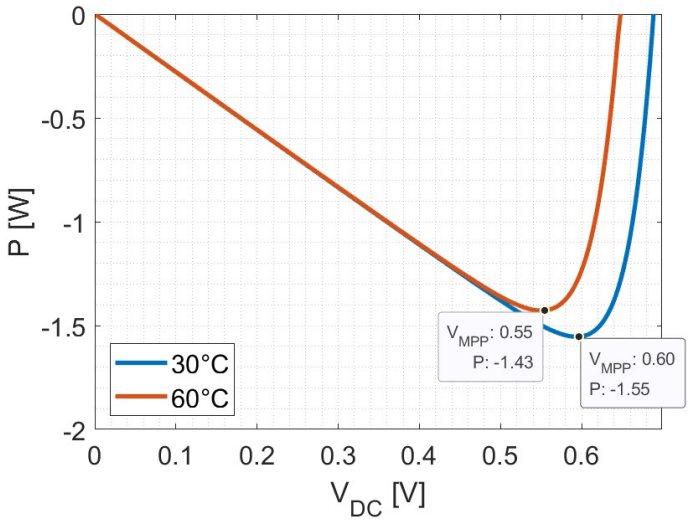

Figure B.6: Effect of the temperature on the power of IBC cell at $500\mathrm{W/m^2}$.

Bibliography

[1] Hannah Ritchie, Max Roser, and Pablo Rosado. "Energy". In: *Our World in Data* (2022). URL: https://ourworldindata.org/energy.

[2] Umair Shahzad. "Global Warming: Causes, Effects and Solutions". In: (Aug. 2015).

[3] A. Smets et al. *Solar Energy: The Physics and Engineering of Photovoltaic Conversion, Technologies and Systems*. UIT Cambridge, 2016. ISBN: 9781906860325. URL: https://books.google.nl/books?id=vTkdjgEACAAJ.

[4] Romênia G. Vieira et al. "A Comprehensive Review on Bypass Diode Application on Photovoltaic Modules". In: *Energies* 13.10 (2020). ISSN: 1996-1073. DOI: 10.3390/en13102472. URL: https://www.mdpi.com/1996-1073/13/10/2472.

[5] Chris Deline et al. "Evaluation of Maxim module-Integrated electronics at the DOE Regional Test Centers". In: *2014 IEEE 40th Photovoltaic Specialist Conference (PVSC)*. 2014, pp. 0986–0991. DOI: 10.1109/PVSC.2014.6925080.

[6] S. Zahra Mirbagheri Golroodbari, Arjen. C. De Waal, and Wilfried G. J. H. M. Van Sark. "Improvement of Shade Resilience in Photovoltaic Modules Using Buck Converters in a Smart Module Architecture". In: *Energies* 11.1 (2018). ISSN: 1996-1073. DOI: 10.3390/en11010250. URL: https://www.mdpi.com/1996-1073/11/1/250.

[7] Jason T. Stauth, Michael D. Seeman, and Kapil Kesarwani. "A Resonant Switched-Capacitor IC and Embedded System for Sub-Module Photovoltaic Power Management". In: *IEEE Journal of Solid-State Circuits* 47 (2012), pp. 3043–3054.

[8] Jagannath Panigrahi et al. "Impedance spectroscopy of crystalline silicon solar cell: Observation of negative capacitance". In: *Solar Energy* 136 (2016), pp. 412–420. ISSN: 0038-092X. DOI: https://doi.org/10.1016/j.solener.2016.06.041. URL: https://www.sciencedirect.com/science/article/pii/S0038092X16302225.

[9] Razman Ayop and Chee Tan. "Design of boost converter based on maximum power point resistance for photovoltaic applications". In: *Solar Energy* 160 (Jan. 2018), pp. 322–335. DOI: 10.1016/j.solener.2017.12.016.

[10] Saeed Rahimpour et al. "An Overview of Lifetime Management of Power Electronic Converters". In: *IEEE Access* 10 (2022), pp. 109688–109711. DOI: 10.1109/ACCESS.2022.3214320.

[11] David A. van Nijen et al. "Exploring the benefits, challenges, and feasibility of integrating power electronics into c-Si solar cells". In: *Cell Reports Physical Science* 3.7 (2022), p. 100944. ISSN: 2666-3864. DOI: https://doi.org/10.1016/j.xcrp.2022.100944. URL: https://www.sciencedirect.com/science/article/pii/S2666386422002259.

[12] Jen-Hung Huang, Brad Lehman, and Ting Qian. "Submodule integrated boost DC-DC converters with no external input capacitor or input inductor for low power photovoltaic applications". In: *2016 IEEE Energy Conversion Congress and Exposition (ECCE)*. 2016, pp. 1–7. DOI: 10.1109/ECCE.2016.7855476.

[13] Admin. *Solar panel connected with a boost converter*. https://latexdraw.com/draw-a-dc-dc-boost-converter-in-latex-using-circuitikz. Accessed: 2023-01-24. 2021.

[14] J.E. Garland et al. "Electro-analytical characterization of photovoltaic cells by combining voltammetry and impedance spectroscopy: Voltage dependent parameters of a silicon solar cell under controlled illumination and temperature". In: *Energy Environ. Sci.* 4 (Feb. 2011), pp. 485–498. DOI: 10.1039/C0EE00307G.

[15] Donald A. Neamen. *Semiconductor Physics and Devices Basic Principles (4th ed.)* McGraw-Hill, 2012. ISBN: 9780073529585.

[16] David A. van Nijen et al. “Revealing capacitive and inductive effects in modern industrial c-Si photovoltaic cells through impedance spectroscopy”. In: *Solar Energy Materials and Solar Cells* 260 (2023), p. 112486. ISSN: 0927-0248. DOI: https://doi.org/10.1016/j.solmat.2023.112486. URL: https://www.sciencedirect.com/science/article/pii/S0927024823003070.

[17] Byoung-Yong Chang. “Conversion of a Constant Phase Element to an Equivalent Capacitor”. In: *Journal of Electrochemical Science and Technology* 11 (June 2020). DOI: 10.33961/jecst.2020.00815.

[18] Jagannath Panigrahi et al. “Impedance spectroscopy of amorphous/crystalline silicon heterojunction solar cells under dark and illumination”. In: *Solar Energy* 259 (2023), pp. 165–173. ISSN: 0038-092X. DOI: https://doi.org/10.1016/j.solener.2023.05.030. URL: https://www.sciencedirect.com/science/article/pii/S0038092X23003626.

[19] RS PRO. *RS PRO Type T Thermocouple 1m Length, 1/0.2mm Diameter → +250°C*. RS PRO. circa 2021. URL: https://docs.rs-online.com/45aa/A700000007350706.pdf.

[20] M.S. Suresh. “Measurement of solar cell parameters using impedance spectroscopy”. In: *Solar Energy Materials and Solar Cells* 43.1 (1996), pp. 21–28. ISSN: 0927-0248. DOI: https://doi.org/10.1016/0927-0248(95)00153-0. URL: https://www.sciencedirect.com/science/article/pii/0927024895001530.

[21] R. Kumar, M. Suresh, and Nagaraju Jampana. “Facility to measure solar cell ac parameters using an impedance spectroscopy technique”. In: *Review of Scientific Instruments* 72 (Aug. 2001), pp. 3422–3426. DOI: 10.1063/1.1386632.

[22] R. Kumar, M. Suresh, and Nagaraju Jampana. “Silicon (BSFR) solar cell AC parameters at different temperatures”. In: *Solar Energy Materials and Solar Cells - SOLAR ENERG MATER SOLAR CELLS* 85 (Jan. 2005), pp. 397–406. DOI: 10.1016/j.solmat.2004.05.017.

[23] Sanjai Kumar, P. Singh, and G.S. Chilana. “Study of silicon solar cell at different intensities of illumination and wavelengths using impedance spectroscopy”. In: *Solar Energy Materials and Solar Cells* 93 (Oct. 2009), pp. 1881–1884. DOI: 10.1016/j.solmat.2009.07.002.

[24] Iván Mora-Seró et al. “Impedance spectroscopy characterisation of highly efficient silicon solar cells under different light illumination intensities”. In: *Energy Environ. Sci.* 2 (6 2009), pp. 678–686. DOI: 10.1039/B812468J. URL: http://dx.doi.org/10.1039/B812468J.

[25] Bernard A. Boukamp. “A Nonlinear Least Squares Fit procedure for analysis of immittance data of electrochemical systems”. Undefined. In: *Solid state ionics* 20.1 (1986), pp. 31–44. ISSN: 0167-2738. DOI: 10.1016/0167-2738(86)90031-7.

[26] Kean Chern Fong, Keith McIntosh, and Andrew Blakers. “Accurate series resistance measurement of solar cells”. In: *Progress in Photovoltaics: Research and Applications* 21 (Nov. 2011). DOI: 10.1002/pip.1216.

[27] J.E. Garland, Daniel Crain, and Dipankar Roy. “Impedance spectroscopy coupled with voltammetry for quantitative evaluation of temperature and voltage dependent parameters of a silicon solar cell”. In: *Solar Energy* 85 (Nov. 2011), pp. 2912–2923. DOI: 10.1016/j.solener.2011.08.029.

[28] W. B. Berry. “Photovoltaic short-circuit minority carrier injection”. In: *Applied Physics Letters* 25.4 (Oct. 2003), pp. 195–196. ISSN: 0003-6951. DOI: 10.1063/1.1655436. eprint: https://pubs.aip.org/aip/apl/article-pdf/25/4/195/7734046/195_1_online.pdf. URL: https://doi.org/10.1063/1.1655436.